A Precise Retinotopic Map of Primate Striate Cortex Generated from the Representation of Angioscotomas

Daniel L. Adams and Jonathan C. Horton
Beckman Vision Center, University of California, San Francisco, San Francisco, California 94143-0730

Shadows cast by retinal blood vessels are represented in striate cortex of the squirrel monkey. Their pattern was exploited to generate a true retinotopic map of V1. For calibration, retinal landmarks were projected onto a tangent screen to measure their visual field location. Next, the retina was warped onto striate cortex, distorting it as necessary to match each retinal vessel to its cortical representation. Maps from four hemispheres of two normal adult squirrel monkeys were created and used to derive expressions for cortical magnification factor (*M*). A mean map was produced by averaging the individual maps. To address the controversial issue of whether the ratio of retinal ganglion cell (RGC) density to *M* is constant at all eccentricities, we stained a retinal whole mount from one of the two monkeys for Nissl substance. A ganglion cell density map was compiled by sampling the concentration of cells at 171 retinal points. Allowance was made for displaced amacrine cells and for the centripetal displacement of RGCs from central photoreceptors. After these corrections the V1 surface area and RGC density were compared at each eccentricity. The cortical representation of the macula was found to be amplified, even beyond the magnification expected from its high density of RGCs. For example, the central 4° of visual field were allotted 27% of the surface area of V1 but were supplied by only 12% of RGCs. We conclude that, in monkey striate cortex, more tissue is allocated per ganglion cell for the analysis of information emanating from the macula as compared with the peripheral retina.

Key words: **blind spot; monocular crescent; retina; blood vessel; flat-mount; ocular dominance column; cytochrome oxidase; magnification factor; anisotropy; displaced amacrine cell; GABA; retinal ganglion cell; cone; macula; Henle fiber layer**

Introduction

Where explorers go, they depict new territory with maps. The first map of any area in the brain was prepared by an ophthalmologist, Tatsuji Inouye (1909). He correlated visual field scotomas with the location of cranial gunshot wounds in survivors of the Russo-Japanese war to compile a map of the visual field representation in the primary visual cortex. Similar studies were conducted in veterans of later wars (Holmes and Lister, 1916; Spalding, 1952; Teuber et al., 1960). More recently, maps have been made by imaging focal occipital lesions in patients with visual field defects (McAuley and Russell, 1979; Kattah et al., 1981; Spector et al., 1981; Horton and Hoyt, 1991). Maps also can be prepared by using positron emission tomography (Fox et al., 1987) or functional magnetic resonance imaging (Sereno et al., 1995; DeYoe et al., 1996; Engel et al., 1997) in normal subjects. The main problem with the maps resulting from these approaches is their limited spatial resolution.

More precise maps can be prepared in animals by recording from cells with microelectrodes. Talbot and Marshall (1941) mapped the occipital surface (operculum) in the macaque and quantified "cortical discrimination" in terms of degrees of visual angle per millimeter of cortex. Daniel and Whitteridge (1961) plotted the reciprocal, "cortical magnification factor," after making electrode penetrations through different regions of striate cortex. They found that cortical magnification fell by several log units from the foveal representation to the monocular crescent representation, reflecting the greater allocation of cortex to central vision. From their measurement of cortical magnification, they predicted the shape of V1 and the layout of its retinotopic map. Subsequent electrophysiological studies have elaborated on their conclusions (Cowey, 1964; Allman and Kaas, 1971; Dow et al., 1981; Van Essen et al., 1984; Rosa et al., 1997).

The resolution of microelectrode recordings is limited by eye movements, receptive field scatter, inaccuracy in plotting receptive fields, and errors in measuring coordinates in the visual field. It is a daunting task to reconstruct multiple electrode penetrations, especially through folded cortex, so that each recording site can be matched accurately with its corresponding visual field locus. As pointed out by Van Essen et al. (1984), the deoxyglucose method is inherently more precise than microelectrode recordings for the construction of a retinotopic map. After [^{14}C]deoxyglucose administration the retina can be stimulated with a ring and ray stimulus to produce a metabolic imprint in the cortex (Tootell et al., 1988). However, deoxyglucose maps cannot be prepared easily from buried, folded cortex. In monkeys much of striate cortex lies hidden in the calcarine fissure, beyond the reach of the deoxyglucose method. This tissue is also inaccessible to optical imaging (Blasdel and Campbell, 2001).

Recently, we have shown that retinal blood vessels are represented in striate cortex of the squirrel monkey (Adams and Horton, 2002). They can be detected by staining flat-mounts of the cortex for cytochrome oxidase (CO) after enucleation of one eye.

Received Nov. 14, 2002; revised Dec. 16, 2002; accepted Jan. 15, 2003.

This work was supported by the National Eye Institute (Grant R01 EY10217 and Core Grant EY02162), That Man May See, The Bunter Fund, and the Lew W. Wasserman Merit Award from Research to Prevent Blindness. The California Regional Primate Research Center is supported by National Institutes of Health Base Grant RR00169. We thank the California Regional Primate Research Center (especially Jenny Short and David Robb). We also thank Davina Hocking and Irmgard Wood for help with tissue processing and Robin Troyer for assistance with animal care and surgery. Philip Sabes, Lawrence Sincich, and Lars Frisén provided valuable comments on this manuscript.

Correspondence should be addressed to Dr. Daniel L. Adams, Beckman Vision Center, University of California, San Francisco, 10 Kirkham Street, San Francisco, CA 94143-0730. E-mail: dadams@itsa.ucsf.edu.

 0270-6474/03/233771-19$15.00/0

In this paper we used this phenomenon to generate a retinotopic map by matching each segment of the retinal vascular tree to its cortical image. The resulting map is extremely accurate, because it is based on alignment between a multitude of cortical and retinal landmarks. It is immune to many sources of error because it is literally a *retinotopic*, rather than a *visuotopic*, map.

With the aid of this retinotopic map, we have addressed a number of questions long debated by cartographers. (1) Is the mathematical expression for cortical magnification factor a complex log function? (2) Is cortical magnification factor equal along the vertical and horizontal meridia? (3) Is local cortical magnification factor equal along isopolar and isoeccentricity contours at any locus in the visual field representation? (4) Is the ratio of retinal ganglion cell (RGC) density to cortical magnification factor a constant at all eccentricities?

Materials and Methods

This paper describes a mean retinotopic map generated from four hemispheres of two normal squirrel monkeys (*Saimiri sciureus*) named Monkey Q and Monkey P. A description of our methods for visualizing the cortical representation of angioscotomas was presented previously (Adams and Horton, 2002). The steps required to create a retinotopic map of striate cortex from angioscotoma representations are described in Results. All experimental procedures were approved by the University of California, San Francisco, Committee on Animal Research.

Retinal ganglion cell density. The left eye of Monkey P was enucleated under general anesthesia with 2% isoflurane. After fixation by immersion in 2% paraformaldehyde, a whole mount was prepared by dissecting the retina from the underlying pigment epithelium (Stone, 1981). Six radial relieving cuts permitted the retina to be mounted on a 3 × 2" subbed slide, photoreceptor side down. It was stained for Nissl substance via an aqueous chrome alum-gallocyanine method (Kiernan, 1990), coverslipped under glycerol, and sealed with nail varnish. A ring and ray pattern was superimposed onto the whole mount, using 14 calibration points determined *in vivo* by projection of retinal landmarks (e.g., vessel crossings, bifurcations) onto a tangent screen. Counting fields were selected in the middle of each compartment (see Fig. 13*D*,*E*) and located at high power, using retinal blood vessels as guides.

A 40× Plan-Apochromat oil immersion lens (Zeiss, Thornwood, NY) and a Spot RT digital camera (Diagnostic Instruments, Sterling Heights, MI) were used to display an image of the RGC layer onto a computer monitor at a net magnification of 2000×. Parafoveally, where the RGC layer was thickest, it was necessary to focus the microscope 60 μm into the retina to visualize the deepest cells. The outline of each RGC nucleus located within a circular field was traced manually onto a sheet of transparent film taped to the monitor screen. Nuclei were drawn only if their center fell within the boundaries of the window printed onto the transparency film. After all cells were identified in a given plane, we focused more superficially, adding nuclear profiles as they came into view. After reaching the inner limiting membrane, we focused back through the tissue to make sure that every nuclear profile was outlined. Then the total number of outlined profiles on the transparency sheet was counted. Sampling windows were 2000 μm^2 at 0.5, 1.5, 3, 4.5, and 6°; 8000 μm^2 at 12°; and 20,000 μm^2 at 20, 28, 41, and 61°. Larger sampling windows were used at higher eccentricity to compensate for the lower density of ganglion cells. The raw counts were converted to cells/mm^2.

Counts were converted from cells/mm^2 to cells/degrees squared. This was done by comparing the distance (in μm) between the fovea and landmarks in the whole mount to their distance (in degrees) measured *in vivo* by projection of landmarks onto a tangent screen. This approach eliminated the issue of postmortem retinal shrinkage. Local retinal magnification factor averaged 161 μm/degree within the central 24°. Beyond this eccentricity, accurate retinal photography and projection of landmarks were impossible. We therefore scaled a wide-angle schematic eye (Drasdo and Fowler, 1974) to our whole mount to derive values for retinal magnification factor of 159 μm/degree at 28°, 149 μm/degree at 41°, and 116 μm/degree at 61°. It is worth mentioning that shrinkage of striate cortex was not measured but was probably negligible because animals were perfused with only 1% paraformaldehyde.

There is a danger of underestimating RGC concentration centrally, because cells are packed so densely in the macula of whole mounts, especially after dehydration. To avoid this pitfall, Wässle et al. (1990) cut out the central retina from whole mounts and prepared serial cross sections. This approach, however, requires a mathematical approximation to account for nuclear fragments (Abercrombie, 1946). Curcio et al. (1987) achieved accurate cell counts in whole mounts by examining unstained, hydrated tissue with Nomarski differential interference contrast (DIC) microscopy. In hydrated tissue the ganglion cell layer remains 50–60 μm thick in the macula, rather than collapsing to 20 μm (Curcio and Allen, 1990). If one avoids shrinkage of the retina, it is possible to obtain accurate ganglion cell counts in the macula of whole mounts. We used an aqueous-based Nissl stain, which allowed us to maintain our retinal whole mount in a hydrated state and to use conventional light-field optics to distinguish cell types.

Displaced amacrine cell density. So that displaced amacrine cells from RGCs could be differentiated, cross sections of squirrel monkey retina from another eye were stained for GABA immunoreactivity (Hendrickson et al., 1985; Hendry et al., 1987; Wässle et al., 1987, 1990). The tissue was postfixed in 2% glutaraldehyde for 24 hr, embedded in plastic, and sectioned at 3 μm. Sections were air-dried on slides, and the plastic was dissolved in NaOH (Lane and Europa, 1965). Then the retina was incubated with ICN Biomedical Clone 5A9 monoclonal anti-GABA antibody (Irvine, CA) for 2 d at a dilution of 1:30. A Vectastain Elite ABC kit (Vector Laboratories, Burlingame, CA) was used to visualize anti-GABA immunoreactivity with a diaminobenzidine peroxidase reaction product.

Monocular crescent. Peripherally, we determined the eccentricity of the monocular crescent border by placing an anesthetized squirrel monkey in a stereotaxic apparatus and using a light source mounted on an arc perimeter. As the light entered the extreme nasal field, we noted when the corneal light reflex appeared at the nasal limbus. This occurred at an eccentricity of 72° from the midline. The animal's interpupillary distance was 18 mm, and the corneal apex was situated 4 mm posterior to the frontal plane defined by the bridge of the nose. In the human and macaque the monocular crescent defined by the ora serrata of the peripheral temporal retina is smaller than the monocular crescent defined by the nasal bridge. Because the squirrel monkey's eyes are set more closely and the nasal bridge is lower, we assumed that the eccentricity of the monocular crescent border corresponded closely to that of the temporal retinal perimeter. The validity of this assumption was tested by determining the fraction of striate cortex occupied by the monocular crescent representation. In squirrel monkey it measured only 3.2% ($n = 4$), whereas in macaque (Horton and Hocking, 1996b) and human (our unpublished data) it measures 5%. It was significantly smaller in squirrel monkey ($p < 0.0001$, Student's two-tailed t test), reflecting the fact that it begins at ~72°, whereas in macaque and human it begins at ~60°.

Results

A retinotopic map from angioscotomas

Figure 1 illustrates the process of mapping the representation of retinal blood vessels in striate cortex for Monkey P. Both retinas were photographed and calibrated by projection of landmarks onto a tangent screen. After removal of the left eye, striate cortex was flat-mounted and stained for CO to visualize the pattern of ocular dominance columns. Emanating from each optic disc representation were 7–10 serpentine lines, representing major blood vessels in the retina. As explained previously (Adams and Horton, 2002), deprivation caused by shadows from retinal blood vessels induces the rearrangement of geniculocortical afferents after birth. The pattern formed by these remodeled geniculocortical afferents can be detected in adults by monocular enucleation, followed by CO staining.

Figure 2 highlights the steps involved in generating a retinotopic map by using cortical angioscotoma representations. A ring

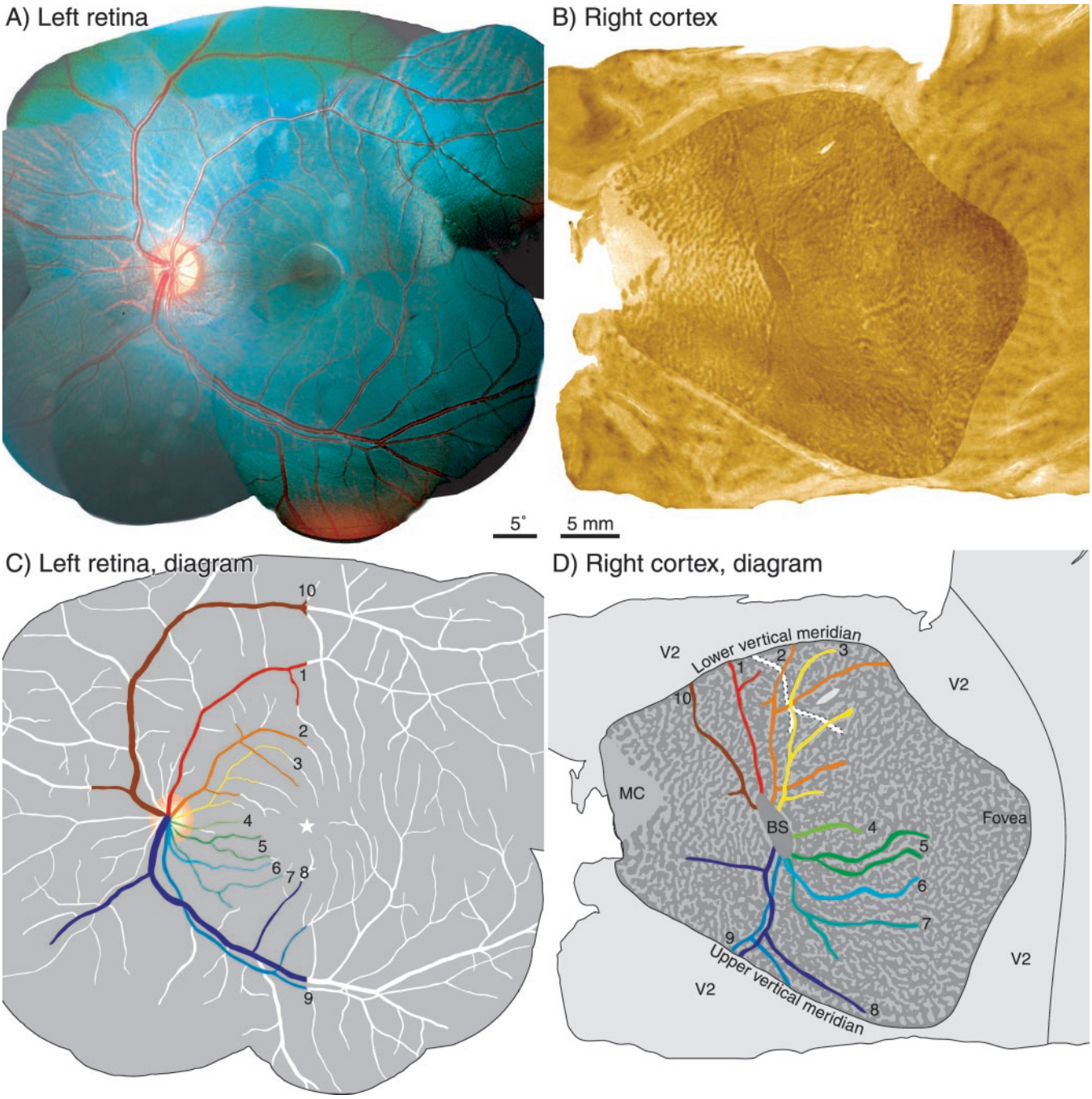

Figure 1. Monkey P. *A*, Montage of retinal photographs. *B*, Flat-mount of cortex, stained for CO after enucleation of the left eye, showing the pattern of ocular dominance columns. The dark lines emerging from the blind spot representation correspond to the cortical representations of retinal blood vessels. Note the CO pattern of alternating pale-thin-pale-thick stripes in area V2. Narrowing of V2 helps to pinpoint the foveal representation. The V1/V2 border corresponds to the vertical meridian of the visual field. *C*, Diagram of blood vessels in *A*, showing in color those represented in the cortex. *D*, Drawing of angioscotoma representations visible in the right cortex above, numbered and color-coded to match retinal vessels in *C*. The white vessel representation outlined with dots was generated by a vessel in the temporal retina of the right eye (not illustrated). BS, Blind spot; MC, monocular crescent; V2, second visual area.

and ray pattern representing the visual hemifield, calibrated in the living animal, was superimposed on the photograph of the nasal retina. Correspondence points, marked with yellow squares, were placed at points at which the location could be determined unambiguously in the retina and the cortex. Ideal correspondence points were provided by vessel bifurcations, crossings, or inflection points. Features such as the borders of V1, the optic disc, and the monocular crescent provided additional retinotopic data.

After correspondence points were identified, they were warped onto the corresponding cortical elements by using a computer program, Elastic Reality 3.0 (Avid Technology, Tewksbury, MA), which performs a linear interpolation between points. The resulting distortion of the ring and ray pattern produced a retinotopic map of each cortex. Each map was based on ~60 correspondence points, plus intercalated segments.

No angioscotomas are represented at eccentricities <4°, because retinal blood vessels become too narrow to cast a dense shadow (Adams and Horton, 2002). Cowey (1964) mapped the central 4°, exposed on the smooth convexity of the squirrel mon-

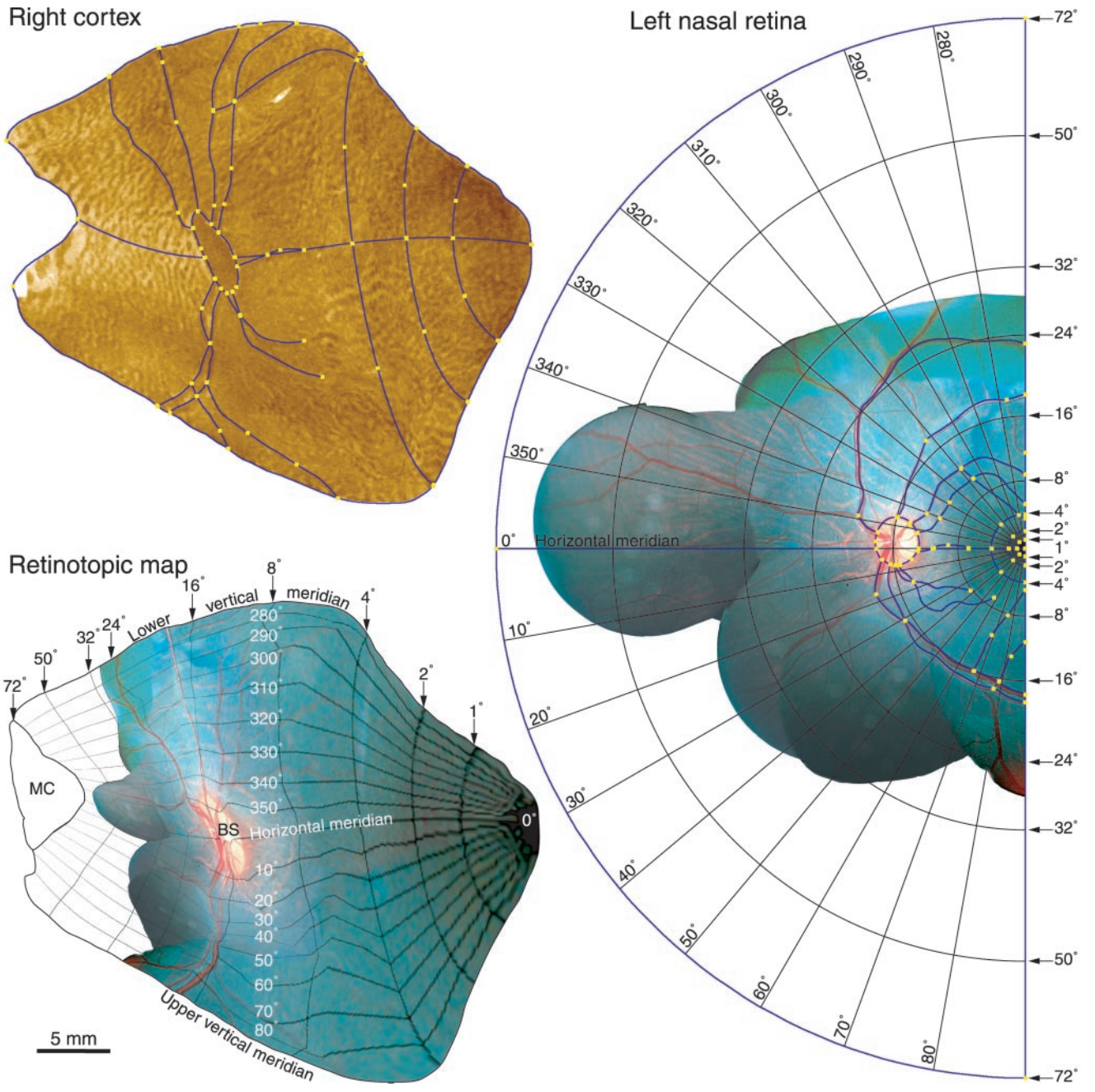

Figure 2. Monkey P. To generate a retinotopic map, we superimposed a ring and ray pattern on the left nasal retina. Correspondence points, marked with yellow squares, were placed at locations that could be identified unambiguously in the cortex and the retina. In this example 64 correspondence points and their intercalated segments were warped from the retina onto the cortex to prepare the retinotopic map. Yellow squares in the central 4° were derived from Cowey (1964).

key occipital cortex, by plotting the receptive field location of 48 electrode recording sites. His detailed retinotopic map of the central 4° was inserted into our map by scaling to the V1/V2 border, fovea, and location of the medial fold of the operculum.

A retinotopic map was prepared from both hemispheres of two monkeys, Monkey Q and Monkey P (Fig. 3). For each map we digitized 172 points, corresponding to each ring–ray intersection. The average map was prepared by reflecting the right cortices onto the left cortices. The individual maps were not scaled or distorted in any way. All four maps were aligned at the fovea (explaining the absence of error bars at the foveal point). They then were rotated to align the point at which the horizontal meridian intersects the monocular crescent (explaining the absence of a vertical error bar at the point marked by the asterisk). We plotted the mean x and y coordinate of each point and connected them with spline curves.

We chose two animals with similar cortical shapes and areas to minimize the size of the error bars. There exists substantial variation from animal to animal in the surface area of striate cortex (Van Essen et al., 1984) and in the shape of striate cortex. Both factors cause variation in the retinotopic map. To construct a maximally precise map, we deliberately chose animals with similar cortices.

The mean map had a surface area of 798 mm^2, close to the average area of squirrel monkey V1 reported previously (Horton and Hocking, 1996a). The monocular crescent occupied 23.5

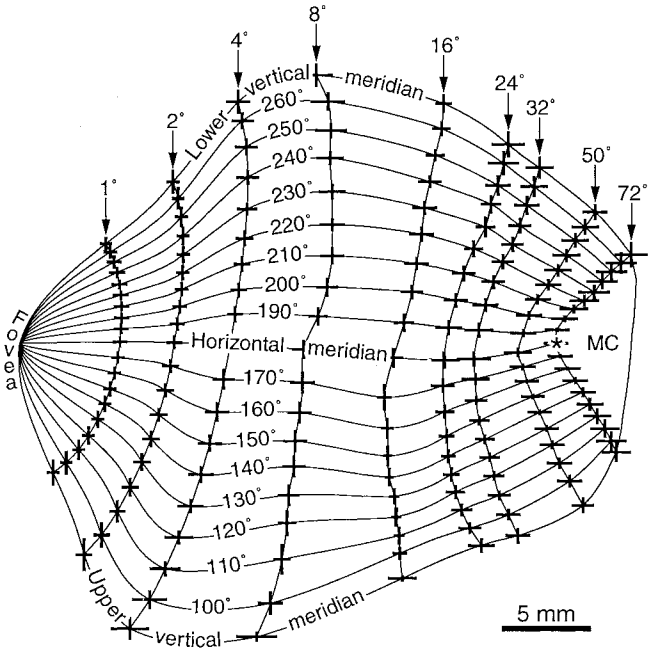

Figure 3. Mean retinotopic map compiled by averaging maps from the left and the (reflected) right striate cortex of Monkey P and Monkey Q [see Adams and Horton (2002), their Fig. 7]. Eccentricity is denoted by the vertical lines representing 1, 2, 4, 8, 16, 24, 32, 50, and 72°. Polar angle is indicated by the horizontal lines from 90 to 270° in 10° intervals. All of the polar rays converge on the foveal representation at the left edge of the map. Error bars indicate ± SEM in the *x*- and *y*-axes. The central 4° are based on data from Cowey (1964).

mm^2, or 2.9% of the total striate area. This was less than in the macaque, in which the monocular crescent averages 5.0% of striate cortex (Horton and Hocking, 1996a). In binocular cortex the upper field quadrant measured 417 mm^2 (54%), and the lower field quadrant measured 357 mm^2 (46%). We found no evidence for a greater representation of the lower field, as suggested for macaques (Van Essen et al., 1984; Tootell et al., 1988). The total perimeter of striate cortex was 104.3 mm. The upper vertical meridian measured 48.5 mm, the lower vertical meridian measured 44.5 mm, and the horizontal meridian measured 30.5 mm (each measured from the fovea to the border of the monocular crescent representation). The vertical meridia were 1.52 times longer than the horizontal meridia. This exceeds the ratio of 1.25 found in the macaque (Daniel and Whitteridge, 1961; Tootell et al., 1988), reflecting the more circular shape of striate cortex in the squirrel monkey.

Cortical magnification factor

The most striking feature of the map was the exaggerated representation of the central visual field. This was quantified by measuring *M*, the cortical magnification factor (Daniel and Whitteridge, 1961). At a particular eccentricity *M* can be measured in two different ways. (1) Areal magnification (M_a) is the cortical surface area devoted to 1 square degree of visual field. Its units are mm^2/degrees squared. (2) Linear magnification is the cortical distance corresponding to 1° in the visual field. Its units are mm/degree. Linear magnification commonly is measured either along a ray (M_p) or a ring (M_e).

To calculate areal magnification, we measured (in mm^2) the cortical surface area of each compartment in each of the four retinotopic maps. Next we calculated (in degrees squared) the area (i.e., solid angle) of each corresponding compartment in the visual field. Dividing the two values gave the areal magnification in mm^2/degrees squared.

To calculate linear magnification along polar rays (M_p), we measured the distance along each ray between two eccentricity rings. This distance was divided by the angle subtended by the corresponding ray segment in the visual field (in degrees). This angle was easy to calculate because each ray is analogous to a longitude line on a globe. For example, the visual angle between the 32° and 16° ring was equal to 16°.

To calculate linear magnification along eccentricity rings (M_e), we measured the distance along each ring between two polar rays (analogous to a latitude line on a globe). This distance was divided by the visual angle subtended by the corresponding ring segment in the visual field (in degrees).

To show how magnification varies over the retinotopic map, we plot M_a, M_p, and M_e against eccentricity in Figure 4. M_a was averaged over all 18 compartments in one-half of a spherical segment and plotted with SE bars at an eccentricity midway between two rings (Fig. 4*A*). Because M_a declines in an approximately logarithmic way, this slightly overestimates M_a but has the advantage of making no assumptions about its mathematical function (see Tootell et al., 1988). M_p was averaged over all 19 ray segments between two neighboring rings and plotted midway between them (Fig. 4*B*). M_e was averaged over all 18 segments along a given ring and plotted exactly at its eccentricity (Fig. 4*C*).

The first map of primary visual cortex, compiled by Inouye (1909), is shown in Figure 5*A*. Polar angle is represented by horizontal lines, and eccentricity is represented by vertical lines. Although Inouye may not have understood its mathematical implications fully (see translation by Glickstein and Fahle, 2000), the map is recognizable as the complex logarithmic transformation of the visual field (Schwartz, 1977, 1980). It is physically impossible, because the fovea is represented as a line. Consequently, cortical magnification approaches infinity as eccentricity drops to 0°. Electrophysiological recordings by Talbot and Marshall (1941) later showed convincingly that the isopolar rays converge to a point at the representation of the fovea. All subsequent maps have agreed on this principle.

Using retinotopic data from different sources, various authors have attempted to model mathematically how *M* varies as a function of eccentricity (Daniel and Whitteridge, 1961; Fischer, 1973; Hubel and Freeman, 1977; Schwartz, 1977; Van Essen et al., 1984; LeVay et al., 1985; Schein and de Monasterio, 1987; Johnston, 1989). The general formula for magnification factor (Van Essen et al., 1984) is:

$$M = a(b + E)^c,$$

where *E* is eccentricity and *a*, *b*, and *c* are constants. The constant *a* is a scaling factor. The constant *b* was introduced by Schwartz (1977). It prevents *M* from climbing to infinity as *E* approaches 0°, thus correcting the error in Inouye's map.

If the visual field map in striate cortex conformed to the complex logarithmic mapping function of Schwartz (1984), the constant *c* would equal −1 for linear magnification and −2 for areal magnification. We fit curves to our data to derive the constants in the magnification factor expression (Fig. 4). Either the value of *c* was restricted to obey the complex logarithmic function, or it was allowed to vary according to the value that yielded the best fit (Van Essen et al., 1984).

The value of *c* for M_p was close to −1, indicating that M_p decreased logarithmically with increasing eccentricity. However, the value of *c* for M_e was less than would be expected for a purely

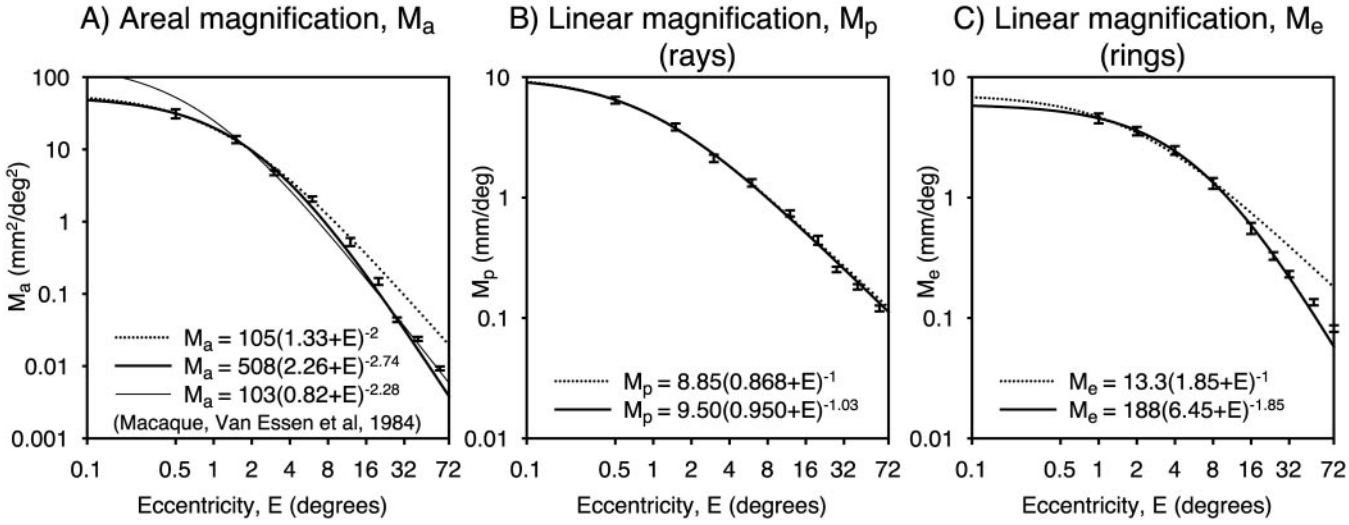

Figure 4. *A*, Cortical areal magnification factor (M_a) as a function of eccentricity. The dotted line represents the equation $M_a = a(b + E)^c$, with c constrained to −2. The heavy solid curve is the best fit of the equation with an unconstrained exponent. The complex log function fits the data well only for the first 8°. Beyond this eccentricity the decline in M_a is greater than that predicted by a conformal map. The thin solid line shows that M_a for the macaque is extremely similar. *B*, Linear magnification along isopolar rays (M_p) as a function of eccentricity. The dotted line represents the equation $M_p = a(b + E)^c$, with c constrained to −1. It is close to the best fit with an unconstrained exponent (solid line). *C*, Linear magnification along isoeccentricity rings (M_e) versus eccentricity. The dotted curve ($c = -1$) deviates from the best fit (solid curve; $c = -1.85$) beyond 8°. Error bars indicate ± SEM of four hemispheres.

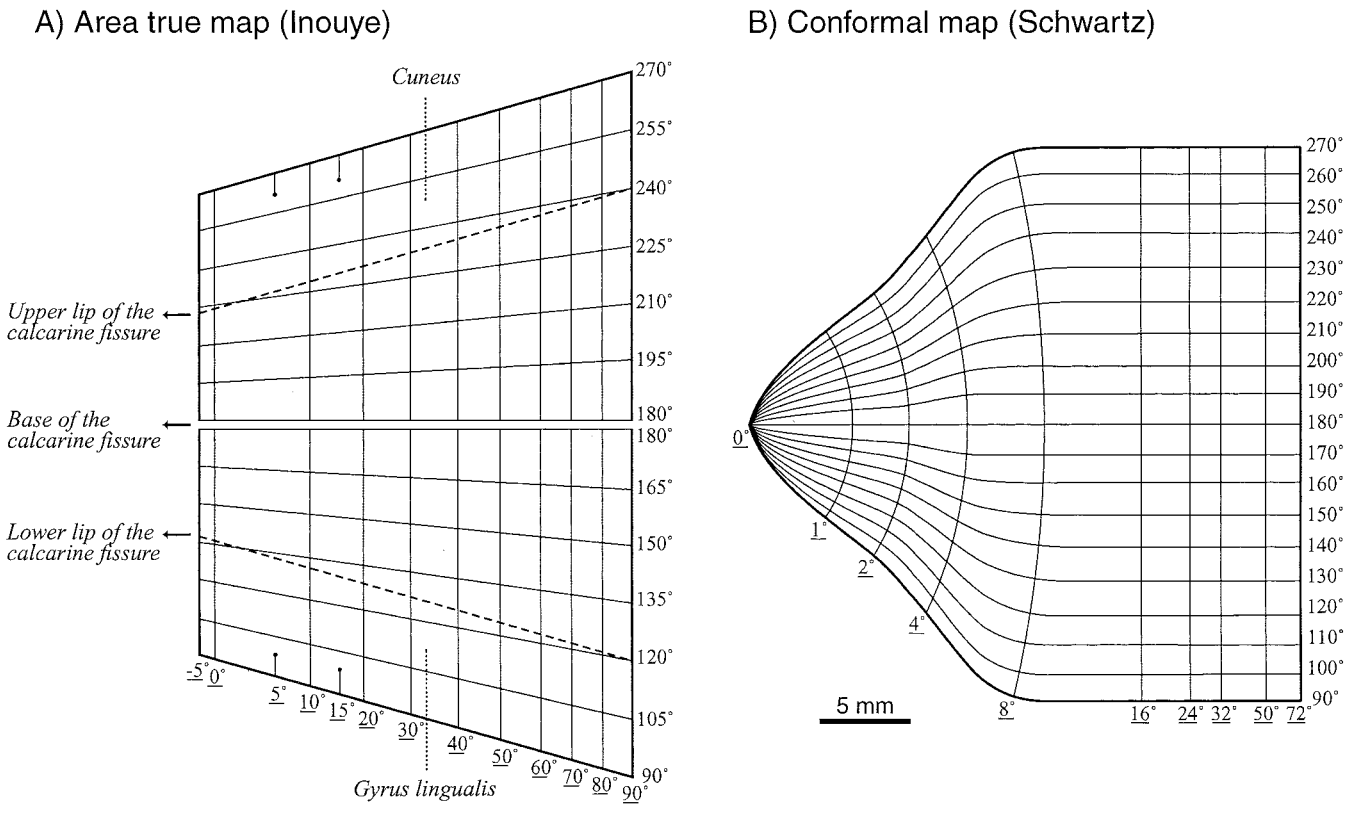

Figure 5. *A*, Inouye's map, published in 1909, appears to show an ideal complex logarithmic mapping of the visual field onto the cortex, although he called it an "area true" map. It appears as a grid, with horizontal lines corresponding to isopolar lines and vertical lines corresponding to isoeccentricity rings (eccentricities are underlined). The map is physically impossible, because the center of gaze (0°) is represented by a line, not a point. *B*, Modified conformal map, after Schwartz (1984), bringing the isopolar rays and isoeccentricity rings to a point at the fovea. In the periphery they remain orthogonal. In reality (Fig. 3), the isopolar rays converge peripherally, and the isoeccentricity rings become curved and shortened.

conformal map. In a conformal map the upper and lower vertical meridia should be parallel in the periphery (Fig. 5*B*). In the squirrel monkey (Fig. 3) the upper and lower vertical meridia draw back together in the periphery after reaching a maximum separation at 8°. This shortens the representation of the isoeccentricity rings, reducing c to less than −1 for M_e and less than −2 for M_a. Macaque V1 has a more oval shape than squirrel monkey V1. Therefore, the vertical meridia are more parallel in the midperiphery. Schwartz proposed that the complex log model fits macaque V1 out to 30°. Beyond that eccentricity the vertical meridia

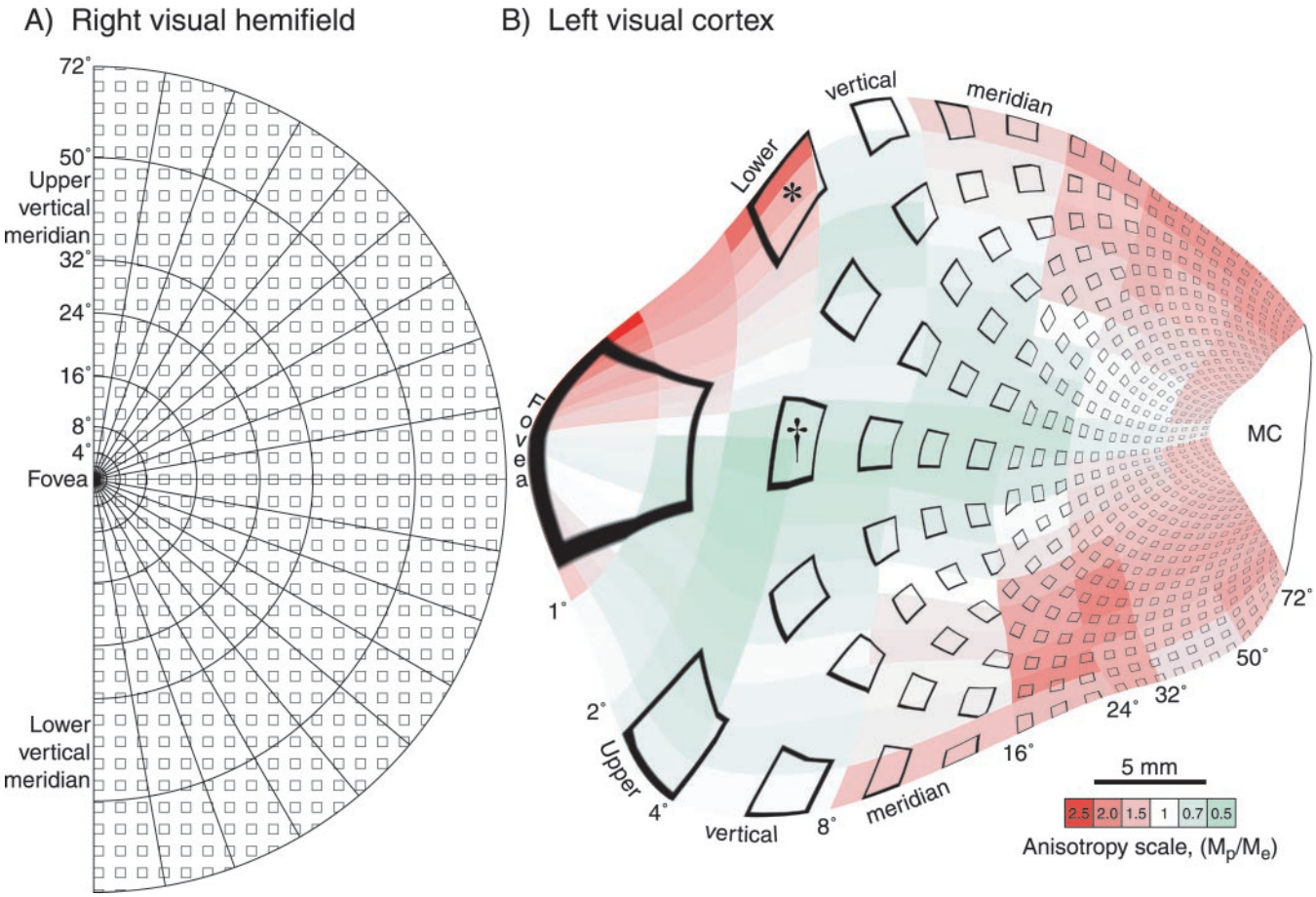

Figure 6. *A*, A field of uniform squares projected onto the visual cortex (*B*), showing the distortion produced by global changes in cortical magnification (M_a) and by local anisotropy. The anisotropy index (M_p/M_e) is depicted by the color scale and ranges from 2.8 to 0.5 (mean, 1.2; SD, 0.4). It tends to be greatest along the vertical meridia and in the periphery. Consequently, squares near the vertical meridia (for example, see asterisk) are elongated along the isopolar direction, whereas those along the horizontal meridian (see dagger) are elongated along the isoeccentricity direction.

converge, so the map deviates from the shape of the theoretical map shown in Figure 5*B* (Schwartz, 1977, 1980, 1983).

In fact, even in macaque the vertical meridia are never truly parallel. As in squirrel monkey, the cortex reaches a maximum width at 8° and then begins to taper (Horton and Hocking, 1996b, 1998). Therefore, even the macaque does not conform to the complex log model. Although one can modify further the equation for cortical magnification factor in an attempt to approximate the actual shape of striate cortex (see Schwartz, 1983), it is doubtful that the visual field representation is governed by any strict mathematical principle in any species.

The cortical map is described as isotropic if values for M_e and M_p are equal at any given locus. The curves in Figure 4, *B* and *C*, depicting mean values for M_e and M_p are not identical. To compare their values, we calculated the anisotropy index, M_p/M_e (Van Essen et al., 1984), for each compartment in the cortical map (Fig. 6). To make this calculation, one must derive values for M_p and M_e at the center of each compartment. For M_p we averaged the value of M_p for two adjacent ray segments. For M_e we divided M_a by mean M_p for each compartment.

Figure 6 shows that the anisotropy index varies systematically across the visual field map. As in the macaque (Van Essen et al., 1984), it tends to be greater along the vertical meridian (mean value, 1.56) than along the horizontal meridian (mean value, 0.88). This occurs because the path length of each polar ray increases systematically the closer its location to the vertical meridian. The anisotropy index also becomes larger at more peripheral eccentricities (e.g., >16°). This occurs because the convergence of polar rays near the monocular crescent representation shortens the isoeccentricity lines, reducing the relative value of M_e.

To illustrate how the anisotropy index affects the representation of the visual field, we projected a field of identical squares onto striate cortex (Fig. 6), using the same warping technique used to create our mean map. Squares near the foveal representation are magnified enormously, as predicted from the M_a ratio of ~10,000:1 from fovea/periphery (Fig. 4*A*). Along the horizontal meridian the squares appear elongated in the cortex, with their long axes generally oriented perpendicular to the horizontal meridian. This distortion (approximately speaking, from squares to rectangular trapezoids) is produced by the decrement in global cortical magnification from center to periphery. Along the vertical meridia the squares also are elongated, but with their long axes parallel to the vertical meridia. Stretching occurs in this direction despite declining global cortical magnification from center to periphery because of the high anisotropy index along the vertical meridian. In squirrel monkey Blasdel and Campbell (2001) have used optical imaging with square wave gratings to show this anisotropy along the vertical meridian.

As mentioned above, higher anisotropy indices result from the greater length of isopolar rays near the vertical meridia. To examine this effect more closely, we graphed M_p versus polar angle between each adjacent pair of isoeccentricity rings (Fig.

7*A*). Each curve is "hammock" shaped; that is, M_p declines toward the horizontal meridian at each eccentricity. M_e increases slightly toward the horizontal meridian (data not shown), thereby maintaining M_a nearly constant at each polar angle (Fig. 7*B*) for a given eccentricity. In simplest terms the map compartments (Fig. 3) are more rectangular near the vertical meridian than near the horizontal meridian, but their net area is quite constant. We did not observe an increase in M_a near the horizontal meridian in our mean map, as reported by Van Essen et al. (1984) for the macaque. However, there appears to be real variability in this property among individual squirrel monkeys, judging from the variation we have observed in the shape of the blind spot representation (oval versus circular) in normal animals.

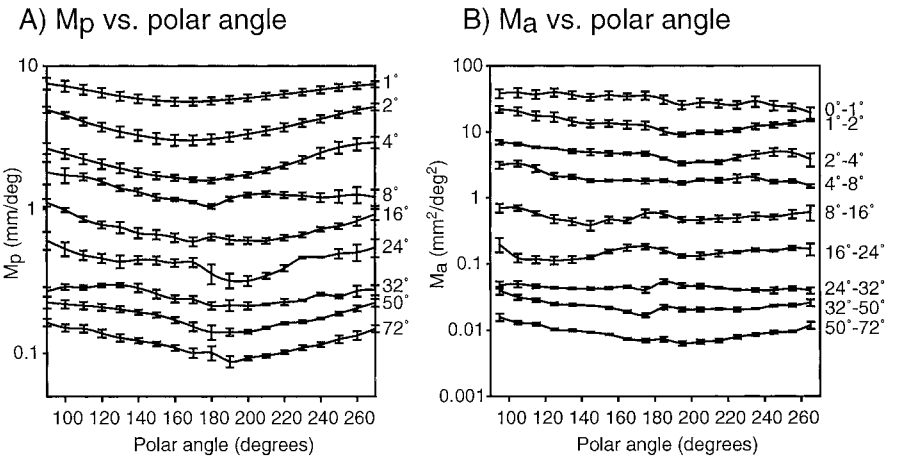

Figure 7. *A*, M_p, graphed as a function of polar angle between each pair of isoeccentricity rings, declines at the horizontal meridian (180°). Graphed points represent the mean of four hemispheres ± SEM. *B*, M_a, plotted for each compartment in the visual field map, remains approximately constant between each pair of isoeccentricity rings. The decline in M_p is offset by an increase in M_e. This effect can be appreciated in the cortical map (Fig. 3). Near the vertical meridia the compartments are rectangular, whereas near the horizontal meridian they are more square. Their area along any isoeccentricity belt, however, is essentially independent of polar angle.

Visual field domain of a cortical patch

In many species, especially primates, striate cortex contains a regular array of cytochrome oxidase patches (Horton and Hubel, 1981; Carroll and Wong-Riley, 1984; Horton, 1984). Farias et al. (1997) have emphasized that in macaques their spatial density is quite constant throughout binocular cortex. The same is true in the squirrel monkey. Figure 8 shows a section through layer 3 from the right striate cortex of Monkey Q, an animal used to prepare our retinotopic map. There were 2534 patches in 792 mm^2 of binocular cortex. The patches seemed to be evenly distributed. To confirm this impression, we measured their density at different eccentricities. It ranged between 2.77 and 3.95 patches/mm^2. By calculating the area of each spherical zone in the visual field, we determined the number of patches/degree squared. These data are graphed in Figure 9. Because the density of patches in the cortex is quite constant, the graph bears a close resemblance to the graph of M_a versus eccentricity (Fig. 4*A*).

The reciprocal of patches/degree squared yields a function called the "blob (patch) domain" (Tootell et al., 1988). This corresponds to the amount of visual field served by a CO patch at a given eccentricity. In the squirrel monkey it ranges from 0.008 degrees squared in the central 1° to 29.3 degrees squared in the periphery (Fig. 9). The most vivid impression of how patch domain varies with eccentricity can be obtained by back-projecting the CO patches (Fig. 8) onto the visual field (Fig. 10). Analogous back-projections have been performed for the ocular dominance columns (Hubel and Freeman, 1977; LeVay et al., 1985). The back-projection was accomplished by warping the cortical image of the patches onto the polar coordinates of the visual hemifield, essentially reversing the process used to create cortical maps (Fig. 2). In the peripheral field the patches are sparse because they each cover a large territory, whereas near the central field they are packed so densely that the image must be magnified to see them. Their distribution mirrors the gradient in M_a. Because the patches vary in their shape and pattern, it is difficult to infer any underlying principle from their local appearance in the visual field projection.

Retinal ganglion cell density

Ganglion cells are the output elements of the retina. Peripherally, the ganglion cell layer contains only a scattering of cells, but centrally it forms a tightly packed sheet, several cells deep. It is controversial if the ratio of RGC density to V1 surface area is constant at all eccentricities (for review, see Pointer, 1986; Tolhurst and Ling, 1988). Previous analyses have been hampered by difficulties in measuring ganglion cell density, compensating for Henle fiber layer displacement, translating retinal points onto the visual field, and mapping accurately striate cortex. To make matters worse, ganglion cell densities derived from one animal have been compared with cortical maps prepared in another, introducing additional variation.

We decided to reexamine the relationship between ganglion cell density and M_a, because our experimental approach has minimized three obstacles mentioned above. First, we made ganglion cell counts in one of the monkeys used to generate our retinotopic map. Second, retinal landmarks were projected onto a tangent screen, allowing us to determine experimentally the visual field coordinates of retinal compartments (some extrapolation was required beyond 24°). Third, the accuracy of our cortical map allowed for valid measurements of M_a.

Figure 11*A* shows a Nissl-stained whole mount of the left retina from one of the two monkeys used to generate the mean map. In the temporal retina the border is visible between the neurosensory retina and the pars plana. In the living squirrel monkey it corresponds to an eccentricity of ~72°. A circle of this radius defines the extent of the visual hemifield seen with both eyes (the binocular visual field). We therefore placed the 72° isoeccentricity ring at this border. Nasal retina located outside this ring serves the monocular crescent of the visual field. It was not included in our analysis.

In Figure 11*B* a montage of fundus pictures (Fig. 1*A*) was superimposed on the whole mount by matching the location of the fovea, optic disc, and major blood vessels. There was a good correspondence between blood vessel landmarks in the whole mount and the photograph. Because these landmarks were calibrated by projection onto a tangent screen, we could use the retinal photograph to determine the location of rings within the central 24°. In this zone retinal magnification factor is nearly constant (Lapuerta and Schein, 1995). In this squirrel monkey we obtained a mean value of 161 μm/degree. Beyond 24° retinal magnification declines because of the optical characteristics of

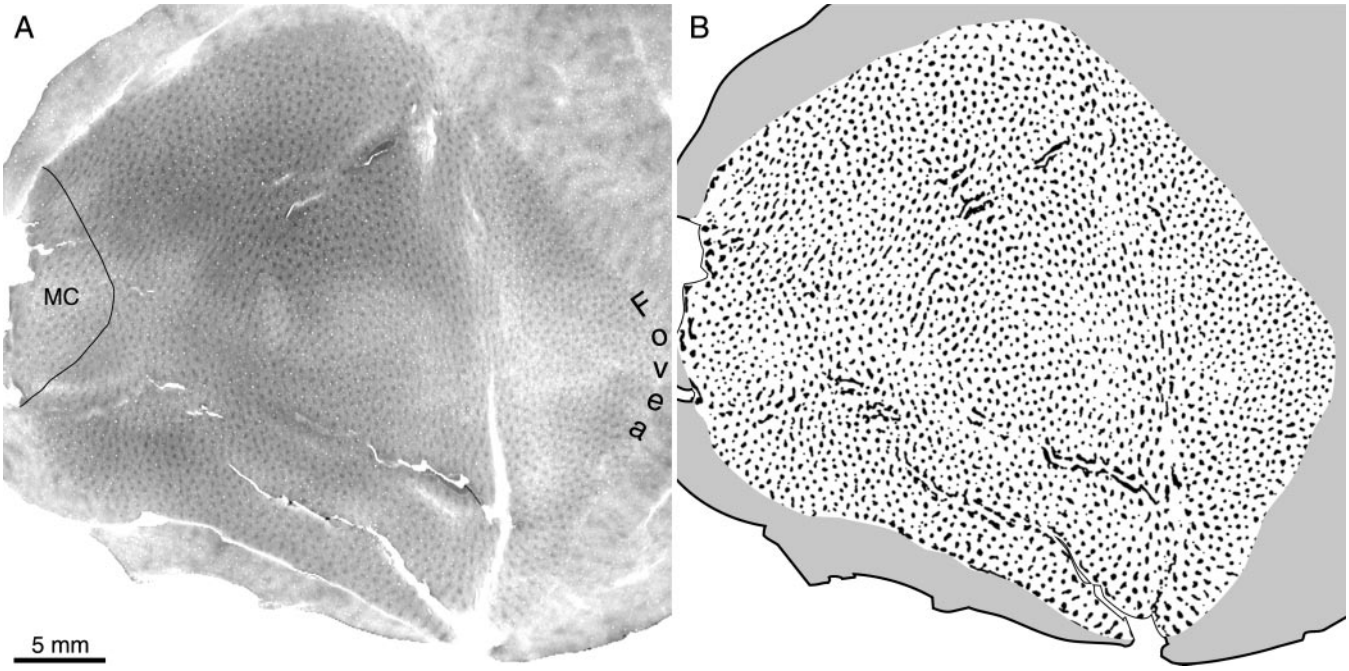

Figure 8. *A*, Single section cut tangentially through a flat-mount of the right visual cortex of Monkey Q, stained for CO to show the patches in the upper layers. This hemisphere was one of four used to compile the retinotopic map in Figure 3. The patches are distributed evenly throughout the cortex. MC, Monocular crescent. *B*, Fourier-filtered and thresholded image of the CO section in *A*, prepared for analysis of patch density and back-projection onto the visual field in Figure 10.

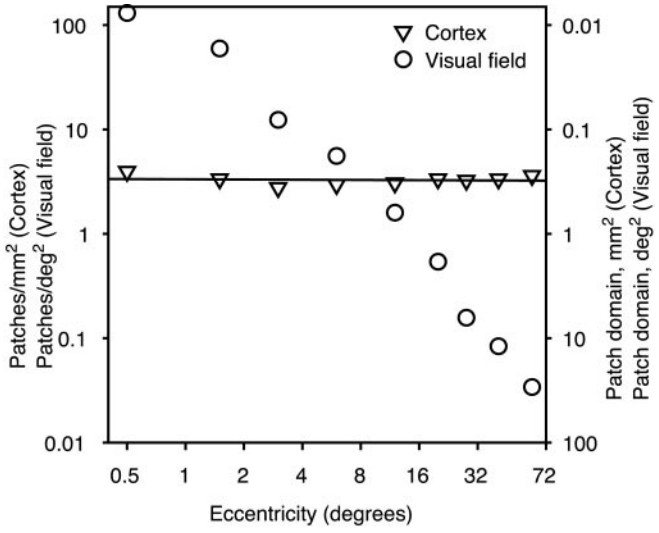

Figure 9. Graph showing patch density for the cortex and its projection onto the visual field (*y*-axis, left) as a function of eccentricity. The reciprocal, patch domain, measured in millimeters squared of cortex per patch or degrees squared in the visual field, is shown also (*y*-axis, right). The number of patches allotted to each square degree in the visual field parallels M_a (Fig. 4*A*), because patch density is quite constant in the cortex.

the eye (Hughes, 1976; Holden and Fitzke, 1988; Bennett et al., 1994). With our fundus camera we could not photograph the peripheral retina or project its blood vessels onto a tangent screen. This made it impossible to locate the 32° and 50° isoeccentricity rings experimentally. Experimental measurement of peripheral retinal magnification factor is an unsolved technical challenge. In the primate there has been only one attempt, making laser lesions at peripheral eccentricities and then examining the retina histologically after enucleation (Frisén and Schöldström, 1977). As an alternative, investigators have relied on ray tracing in schematic eyes to project the peripheral visual field onto the retina. We used a widely accepted model of the optical function of the eye, the wide-angle schematic eye of Drasdo and Fowler (1974), to position the 32° and 50° isoeccentricity rings. This was done by scaling Drasdo and Fowler's projection of the visual field [see Drasdo and Fowler (1974), their Fig. 6] to the retina illustrated in Figure 11*B*.

The ring–ray pattern was superimposed onto the retina, allowing us to establish the relationship between coordinates in the visual field and physical location on the whole mount (Fig. 11*C*). In the far periphery, where relieving cuts were located, it was necessary to bend the rays. To accomplish this, we split the ray pattern down the middle of each relieving cut. Then the seams were warped, contracting the peripheral rays onto the retina (Fig. 11*D*).

Figure 12 shows representative fields of cells at 0.5, 6, 20, and 61°. Ganglion cells are recognizable by their large round nuclei, prominent nucleoli, and relative size (DeBruyn et al., 1980; Leventhal et al., 1981; Stone and Johnston, 1981; Perry et al., 1984). They can be differentiated easily from spindle-shaped endothelial cells lining blood vessels. Astrocytes and microglia are rarely present in the ganglion cell layer (Curcio and Allen, 1990). At any given eccentricity they are smaller than ganglion cells and have an oval, dark nucleus without a prominent nucleolus. Ganglion cell density was sampled at 162 locations, between each pair of isoeccentricity rings at every 20° of polar angle (see yellow dots in Fig. 11*D,E*). The size of the counting window was adjusted with eccentricity so that greater areas of retina were sampled peripherally where cell density is less. In total, 13,616 cells were counted throughout the retina. The peak ganglion cell density was between 3 and 6°. To sample this interval more closely, we made nine additional cell density measurements at 4.5°.

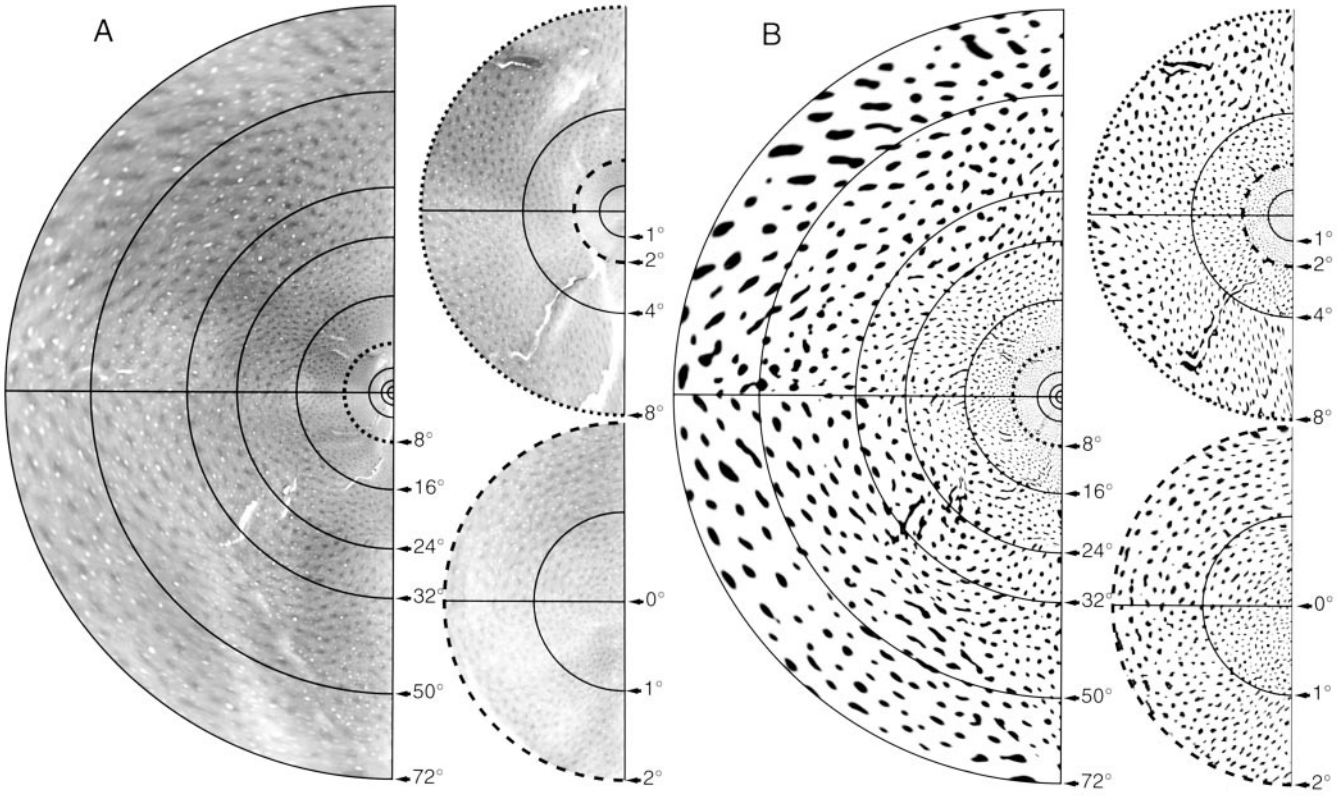

Figure 10. *A*, Back-projection of Figure 8*A* onto the visual field, showing how patch domain varies as a function of eccentricity. Each patches covers a wide domain in the periphery, but centrally the domains are so small that the image must be magnified selectively (right). *B*, Back-projection of Figure 8*B* onto the visual field.

Displaced amacrine cells

Displaced amacrine cells are indistinguishable from ganglion cells in Nissl and therefore contaminated our counts. It was necessary to adjust the raw ganglion cell counts to correct for them. This was done by GABA immunostaining the displaced amacrine cells in a different retina and subtracting their proportion from the ganglion cell counts obtained at each eccentricity. A belt of retina from the fovea to the nasal pars plana was cut from a whole mount. The 2 × 10 mm piece of retina was folded in half, embedded in plastic, sectioned at 3 μm, and processed for GABA.

Figure 13 shows a single immunostained section passing through the fovea and the optic disc. The inner plexiform layer was heavily labeled. Contrary to a previous study in the squirrel monkey showing homogeneous labeling (Brecha, 1983), there were three distinct bands of heavy immunoreactivity, as described in the macaque (Hendrickson et al., 1985; Nishimura et al., 1985). Darkly labeled cells were present in both the inner nuclear layer and the ganglion cell layer (Koontz et al., 1989; Grünert and Wässle, 1990; Koontz and Hendrickson, 1990; Wässle et al., 1990; Crooks and Kolb, 1992). GABA immunohistochemistry is useful for identifying displaced amacrine cells, because 90% stain positively (Wässle et al., 1990; Koontz et al., 1993), whereas ganglion cells are nonreactive (Grünert and Wässle, 1990; Wässle et al., 1990). We counted displaced amacrine cells and ganglion cells at nine eccentricities, centered between isoeccentricity rings, using a 40× oil immersion objective with DIC. The mean proportion of GABA-positive cells at each eccentricity was determined by examining 11 sections, spaced 150–200 μm apart. For the 12° measurement only six sections were examined because the optic disc was present in five sections. We measured displaced amacrine cell proportion, rather than absolute density, eliminating the need for correction factors that are required when cells are counted in cross sections (Abercrombie, 1946).

Four examples of counting windows are shown in Figure 13*A–D*. The amacrine cells constituted a variable percentage of the ganglion cell layer at each eccentricity: 0.5° (0%), 1.5° (4.7%), 3° (3.5%), 4.5° (5.5%), 6° (7.6%), 12° (21.1%), 20° (23.0%), 28° (26.9%), 41° (22.9%), 61° (23.1%). The raw ganglion cell density was multiplied by the proportion of displaced amacrine cells to obtain the corrected ganglion cell density between each pair of isoeccentricity rings (Fig. 14).

Centrifugal displacement of ganglion cells in the macula

The primate fovea is highly specialized to maximize visual acuity. One of its principal adaptations is the centrifugal displacement of inner retinal elements, allowing photoreceptors unimpeded access to rays of light. The axons of photoreceptors fan out radially from the fovea to contact parafoveal bipolar cells, forming the Henle fiber layer of the macula. Bipolar cell axon terminals also are displaced centrifugally, contacting ganglion cells at an even greater eccentricity. The net result is that a photoreceptor located at 0.5°, for example, supplies a ganglion cell situated at 2.5°. Calculation of ganglion cell density in the retina cannot be related meaningfully to visual eccentricity without correcting for this displacement (Boycott et al., 1987; Perry and Cowey, 1988). To perform this correction, we measured the displacement of ganglion cells from their respective photoreceptors in the right retina from the animal whose RGCs we counted, one of the two monkeys used to make the mean retinotopic map (Adams and Horton, 2002).

Under general anesthesia and neuromuscular blockade, the right eye was photographed and landmarks were projected onto a tangent screen for eccentricity calibration. Then the right eye was

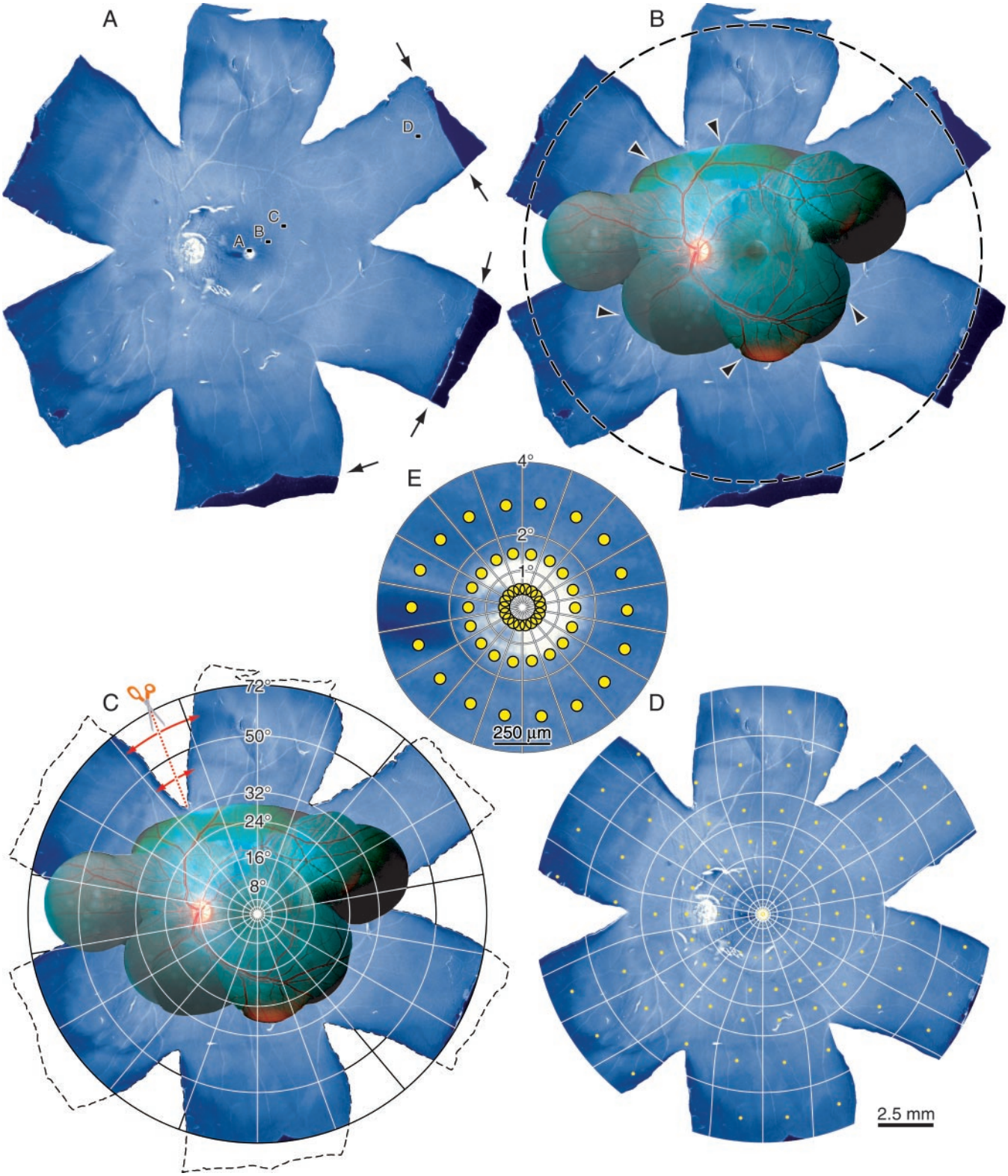

Figure 11. *A*, Nissl-stained whole mount of the left retina of Monkey P. Arrows show boundary between retina (blue) and pars plana (dark brown) in peripheral temporal retina. Lettered boxes are shown at higher power in Figure 12. *B*, Superimposed fundus montage showing the appearance of the retina *in vivo*. When we scaled the picture to match the location of the optic disc, fovea, and blood vessels (arrows) in the whole mount, it was possible to transfer the eccentricity of retinal landmarks measured *in vivo* onto the whole mount to determine the location of the central isoeccentricity rings. The dashed circle, tangential to the edge of the temporal retina, corresponds to the limit of binocular visual field (72°). *C*, Ring and ray pattern, superimposed on the whole mount, using empirical measurements for 0, 1, 2, 4, 8, 16, 24, and 72° rings and the Drasdo and Fowler (1974) schematic eye for the 32 and 50° rings. Red arrows show how the location of the peripheral rays was warped onto the retina to compensate for relieving cuts. *D*, Final registration of the visual field and the retinal whole mount. The yellow dots mark the location of 162 counting windows in which ganglion cell density was measured. Their size accurately represents the area of retina that was examined (see Materials and Methods). *E*, Enlargement of the central 4°.

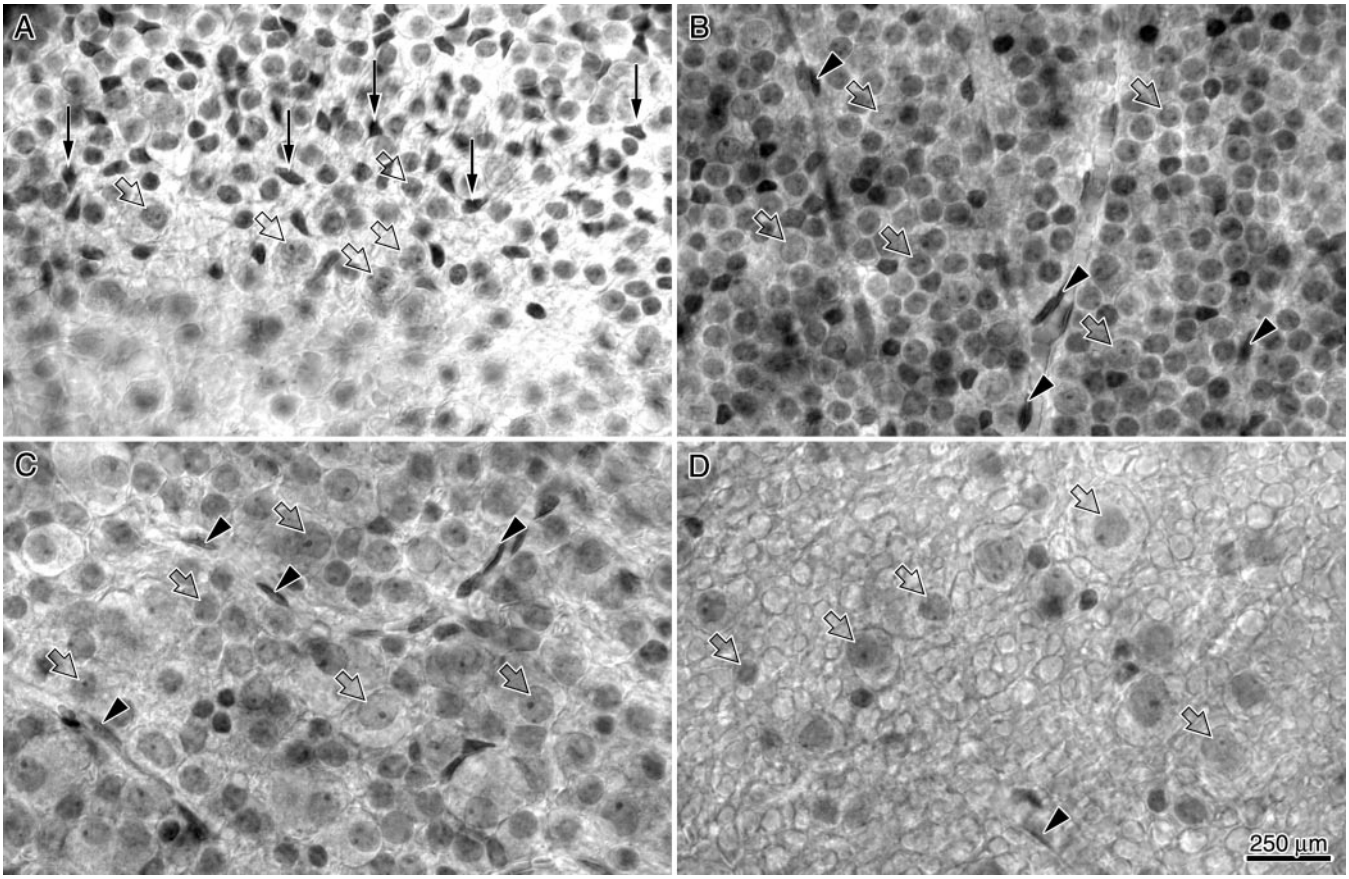

Figure 12. Representative fields of Nissl-stained ganglion cells from locations shown in Figure 11*A*. The appearance of the ganglion cell layer depends critically on eccentricity. At all eccentricities the ganglion cells (open arrows) can be recognized on the basis of their relative size, large nucleus, and prominent dense nucleoli. *A*, A 0.5° field, at the edge of the foveal pit (lower half), where ganglion cells are small and form a monolayer. A few microglia, identifiable by their densely stained irregularly shaped nuclei, are indicated with filled arrows. *B*, A 6° field just beyond the peak density of ganglion cells. The ganglion cells are small and packed four to six cells deep. It was necessary to focus up and down through the ganglion cell layer to count them accurately. Outside the fovea the blood vessels perfuse the ganglion cell layer. Their endothelial cells (arrowheads) could be recognized easily and excluded. *C*, A 20° field showing that the ganglion cells are larger, less numerous, and organized into a single layer. *D*, A 61° field showing the largest cells, scattered widely in the ganglion cell layer.

enucleated, the anterior segment removed, and the fundus rephotographed *in vitro* (Fig. 15*A*). A ring pattern was superimposed onto the retina, calibrated with vascular landmarks identified before enucleation. Serial plastic 1 μm sections were cut along the vertical meridian through the fovea and stained with toluidine blue. Figure 15*B* shows a single section, cut along the vertical white line in the retinal photograph. Three major vessels are indicated by colored arrows. They could be identified clearly in the retinal photograph. To translate eccentricities on the tissue section from millimeters to degrees (thereby eliminating the problem of postmortem tissue shrinkage), we matched these blood vessels to their location in the calibrated retinal photograph.

We then measured the displacement of ganglion cells from their photoreceptors located at 1, 2, 4, and 8°. Applying the approach used by Schein (1988), we followed single fibers from photoreceptor nuclei through the Henle fiber layer to their pedicle in the outer plexiform layer (Fig. 15*C*). It was seldom possible to follow a single fiber the entire distance, but adjacent fibers followed a similar "grain," allowing us to trace their trajectory accurately. Our measurements were made along only one dimension, the inferior vertical meridian. Perry and Cowey (1988) have shown that the Henle fibers are slightly longer in nasal retina than temporal retina, with those along the vertical meridian being intermediate in length. Thus our decision to sample along the vertical meridian was designed to provide a measurement of the mean displacement from photoreceptor to bipolar cell.

A small additional correction must be allowed for the radial displacement of bipolar cell axons onto ganglion cells (Polyak, 1941; Perry and Cowey, 1988; Schein, 1988). These axons could not be traced in our tissue cross sections. To estimate the displacement, we projected the long axis of the oval-shaped bipolar cells directly to the middle of the ganglion cell layer (Fig. 15*C*). This resulted in an additional 10% displacement. Perry and Cowey (1988) have measured this displacement in Golgi preparations of macaque retinal whole mounts and found that it accounts for 10% of the total photoreceptor-to-ganglion cell displacement, consistent with our estimate. Figure 16 shows the relationship between the eccentricity of photoreceptors and their corresponding ganglion cells in the squirrel monkey.

Relation between M_a and ganglion cell density as a function of eccentricity

We have calculated the density of ganglion cells in the retina (Fig. 14) and the displacement of ganglion cells from their photoreceptors (Fig. 16). By combining these data sets, we found that it is possible to correct for the displacement of ganglion cells to determine their functional density versus eccentricity. Via the principles elaborated by Schein (1988), the ganglion cells, in effect, must be shifted centrally into smaller annuli. The result is a mea-

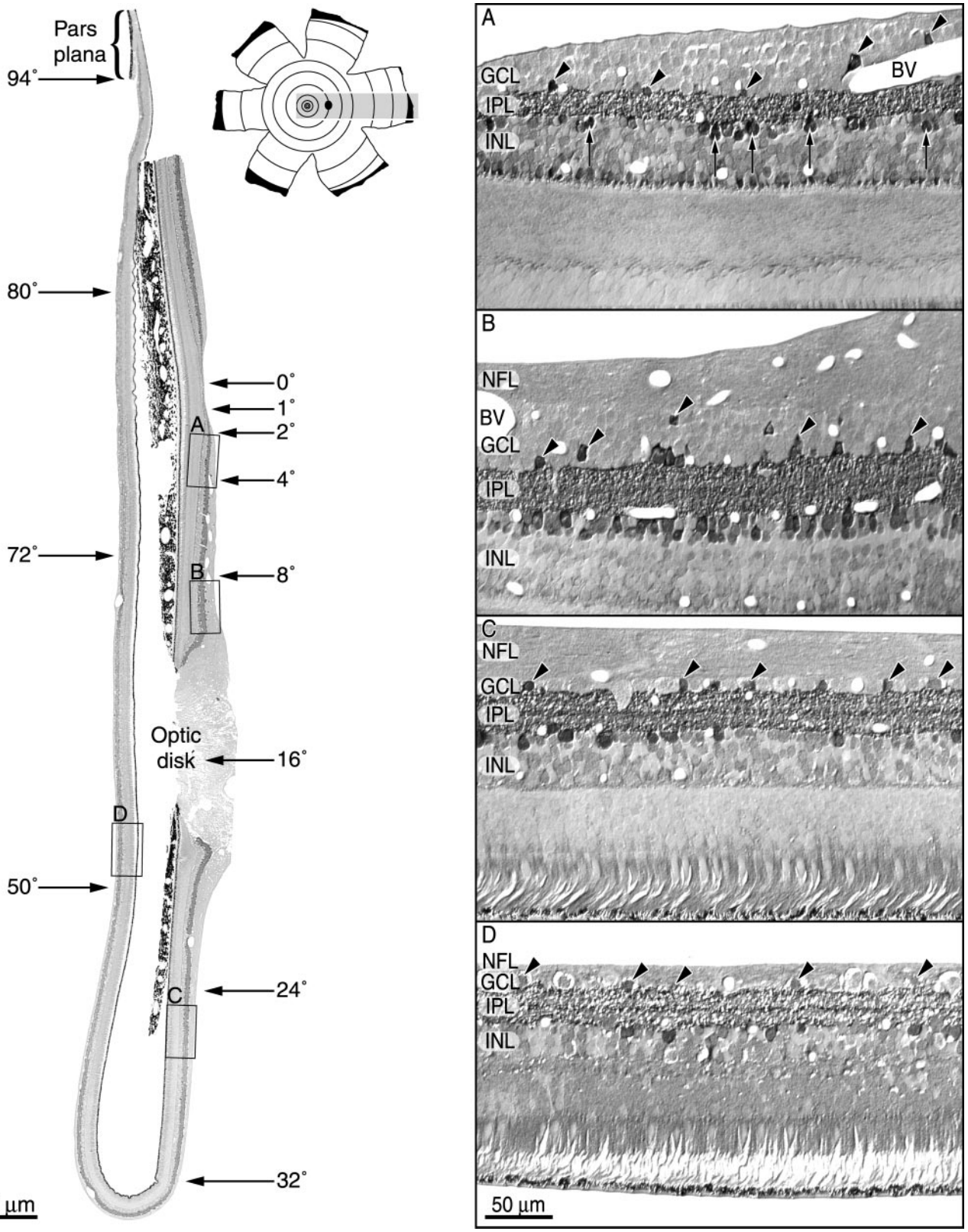

Figure 13. Single 3 μm plastic cross section of squirrel monkey retina, immunoreacted for GABA, to identify displaced amacrine cells in the ganglion cell layer. It was cut from the piece of retinal tissue shaded in the whole mount schematic (inset). The tissue was folded with the nerve fiber layer facing outward before embedding. Rectangles marked with letters are shown at higher power to the right. A DIC oil immersion 40× objective was used to visualize unstained and immunostained cells. *A*, Parafoveal retina containing a high density of ganglion cells, which are unstained. A few GABA-positive cells (arrowheads), stained by the peroxidase reaction used to identify displaced amacrine cells, are present in the ganglion cell layer right next to the inner plexiform layer. Amacrine cells are also present in the inner nuclear layer (long arrows). *B*, Retina at 8–10°, showing a greater number of displaced amacrine cells. Note that the nerve fiber and inner plexiform layers are much thicker than near the fovea. *C*, Retina at ~25°. The ganglion cell layer is reduced to single cell thickness and contains ~25% displaced amacrine cells. The three GABA-positive bands in the inner plexiform layer are particularly prominent at this eccentricity. *D*, Retina at 52°, showing a similar proportion of amacrine cells to those present at 25°. The overall intensity of GABA immunoreactivity declined in peripheral retina. NFL, Nerve fiber layer; GCL, ganglion cell layer; BV, blood vessel; IPL, inner plexiform layer; INL, inner nuclear layer.

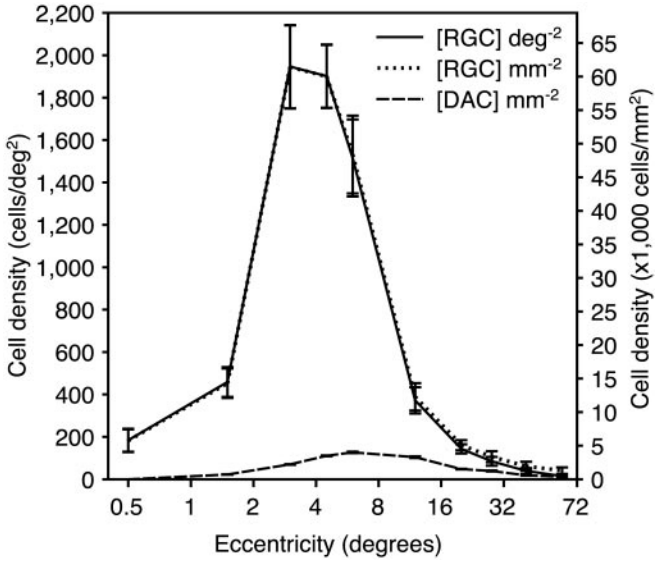

Figure 14. Plot of true ganglion cell and displaced amacrine cell density as a function of retinal eccentricity. Cell densities in the ganglion cell layer were sampled at the points shown in Figure 11, *D* and *E*; displaced amacrine cell densities were calculated from their proportion in the ganglion cell layer, which was determined from analysis of GABA-immunostained sections (see Fig. 13). Displaced amacrine cell densities were subtracted from cell densities in the ganglion cell layer to derive ganglion cell densities at each eccentricity. This "true" ganglion cell density (per mm^2) was averaged over 360° of polar angle. It also is plotted in units of cells/degrees squared, using the retinal magnification factor derived from the schematic eye of Drasdo and Fowler (1974). Error bars indicate ± SEM.

sure of retinal output (*effective* ganglion cell density) at each eccentricity. This calculation was done in stages, as described below:

First, the centrifugal displacement from photoreceptors to their ganglion cells was applied to the isoeccentricity rings as follows: 1° ring → 3.10°, 2° ring → 4.05°, 4° ring → 5.45°, 8° ring → 9.25° (Fig. 16). This step translated the isoeccentricity rings from their optical position in the photoreceptor layer to their effective position in the ganglion cell layer. The rings beyond 8° were not expanded because they fell outside the region of centrifugal displacement of ganglion cells.

Second, the number of cells between the new, displaced locations of the isoeccentricity rings in the ganglion cell layer was calculated. This number was the product of the retinal surface area of each annulus (mm^2) and the mean density of ganglion cells within that annulus (cells/mm^2). Surface area was measured directly from the retina in Figure 11*D*, and mean ganglion cell density was taken from the graph in Figure 14.

Third, the number of ganglion cells obtained in step 2 was divided by the area (mm^2) of the corresponding annulus between undisplaced isoeccentricity rings, yielding the effective density of ganglion cells as a function of visual field eccentricity.

The result of these three steps is shown in Table 1 and graphed in Figure 17. The transformation produced a huge increase in the effective density of ganglion cells centrally. For example, only 488 ganglion cells were located physically within the central 1°, but 25,605 ganglion cells received their input from photoreceptors lying within this zone. The actual density of 5743 cells/mm^2 (488 cells/0.085 mm^2) increased to an effective density of 301,259 cells/mm^2 (25,605/0.085 mm^2). The 1–2° annulus contained 3665 ganglion cells, but its photoreceptors supplied 35,258 cells, a density increase from 14,316 to 137,727 cells/mm^2. More peripheral annuli were affected less, because the displacement of photoreceptors from ganglion cells was smaller. The effective density of ganglion cells in the 4–8°and 8–16° annuli actually declined, because correction for the displacement transferred more cells out of the annuli than in.

There were just over a million ganglion cells in the squirrel monkey retina, close to the number in macaques and humans (Perry et al., 1984; Wässle et al., 1989; Curcio and Allen, 1990). Table 1 shows the percentage of the total ganglion cell population serving each annulus in the visual field. For example, ~12% (2.5 + 3.4 + 6.4%) of the ganglion cells was devoted to representing photoreceptors located in the central 4° of the visual field. Approximately 30% of the ganglion cells served the central 8°.

Is the fraction of ganglion cells situated between each pair of isoeccentricity rings equal to the fraction of surface area corresponding to that annulus on the cortical map? If so, each RGC possesses a constant areal domain in striate cortex, regardless of its eccentricity. We measured the surface area (mm^2) of each annulus in the mean map (Fig. 3). These data were compared with the effective ganglion cell number in each annulus (Table 1). Fig. 18 shows the cumulative percentage of ganglion cells and cortical surface area as a function of increasing eccentricity. The percentage of ganglion cells within each annulus does not equal the percentage of surface area occupied by its corresponding annulus in the cortical map. For example, the cortical representation of the macula accounts for a greater percentage of surface area than one would predict from its percentage of ganglion cells. Specifically, the central 8° of the visual field occupies approximately one-half (48%) of striate cortex, yet the central 8° of retina contains only approximately one-third (30%) of the ganglion cells. The central 4° occupies 27% of the cortex but accounts for only 12% of the ganglion cells.

Discussion

Over the past century neuroscientists have toiled to compile an accurate retinotopic map of the primary visual cortex. This effort has been motivated by a conviction that a more exact map will lead to a better understanding of how the brain converts the external world into an internal representation for visual perception. In this paper we analyzed a mean retinotopic map derived from the representation of the vascular tree of the retina in the primary visual cortex of the squirrel monkey (Adams and Horton, 2002).

From this map several new insights have emerged. We derived mathematical expressions for cortical magnification factor along isopolar and isoeccentricity coordinates of the visual field map. Analysis of these functions showed that a modified complex logarithmic function (Schwartz, 1984) described accurately the cortical magnification along isopolar rays but overestimated the cortical magnification along isoeccentric rings. A map of local anisotropy (M_p/M_e) in the cortical representation of the visual field was compiled, which showed a distinctive pattern of distortion related to systematic differences in M_p and M_e along the vertical versus horizontal meridia. The CO patches in the cortex were back-projected onto the visual field to determine patch domain and density at each eccentricity. Finally, we sampled ganglion cell density at various eccentricities, using the retina from an animal whose cortices contributed to our generation of the mean map. Appropriate corrections were made for displaced amacrine cells and for centrifugal displacement of ganglion cells from their photoreceptors. Comparison of cortical magnification with ganglion cell density showed that the cortical territory corresponding to each ganglion cell is not constant at all eccentricities. Approximately twice the cortical tissue is devoted to the processing of visual information emanating from ganglion cells

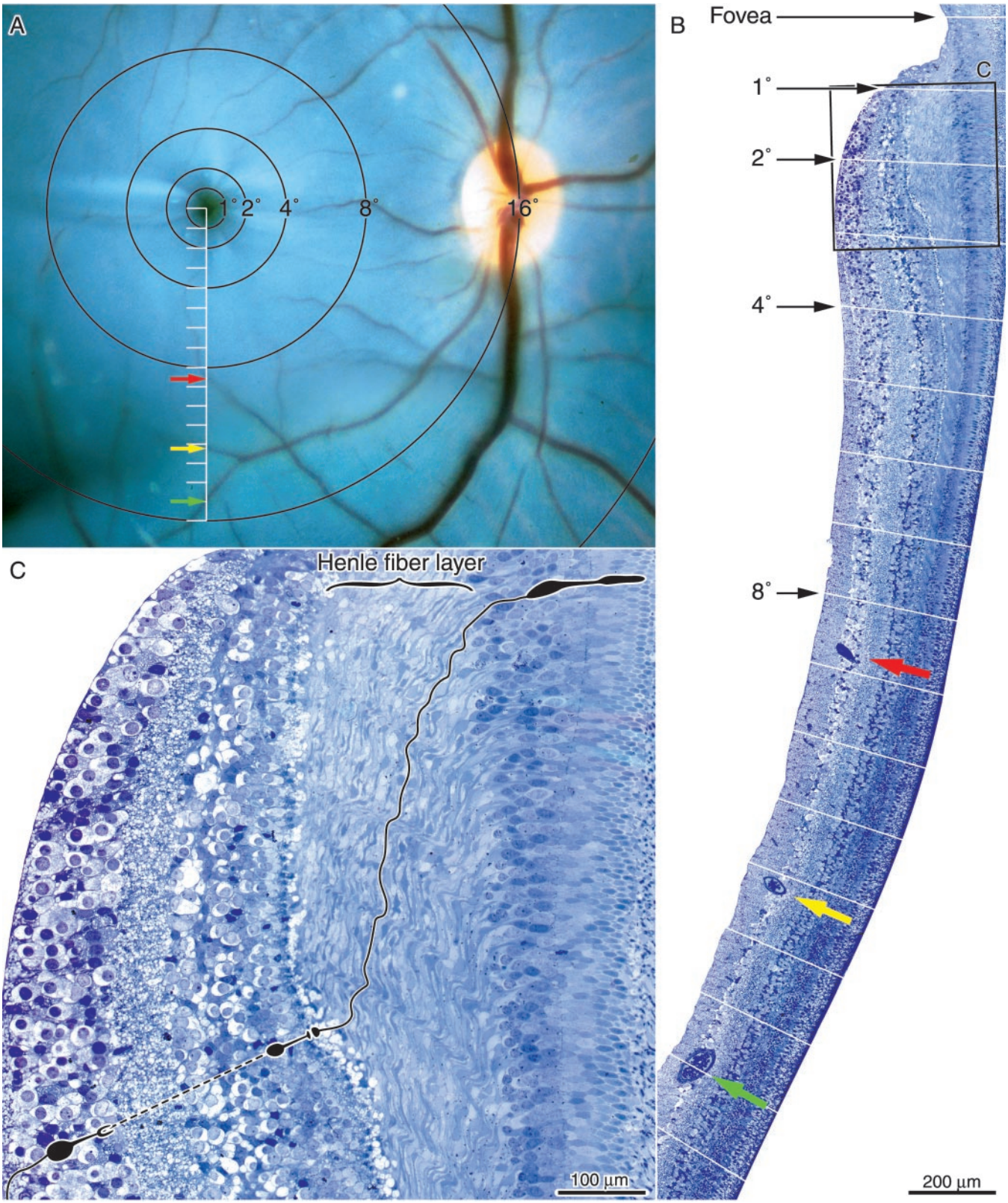

Figure 15. *A*, *In vitro* photograph of the right macula of Monkey Q, showing measurement of the centrifugal displacement from photoreceptors to their target ganglion cells. After enucleation the retina was photographed, embedded in plastic, and sectioned at 1 μm along the vertical meridian through the fovea (white line; divisions = 1°). *B*, Lower portion of a 1 μm cross section, including the fovea and three major vessels marked with red, yellow, and green arrows. These same three vessels are indicated in the retinal photograph with colored arrows. The boxed region is shown in the next panel. *C*, Higher magnification view of the central 1–3°. To illustrate how the centrifugal displacement of ganglion cells from their photoreceptors was measured, we have drawn a schematic example of three cells in the chain. The axon from a single cone at 1° follows a long radial course in the Henle fiber layer (solid line). It terminates on a bipolar cell at 2.8°, which projects to a ganglion cell at 3.1° (dashed line). Measurements of the displacement at 1, 2, 4, and 8° were made independently by both authors. These agreed within 5% and therefore were averaged.

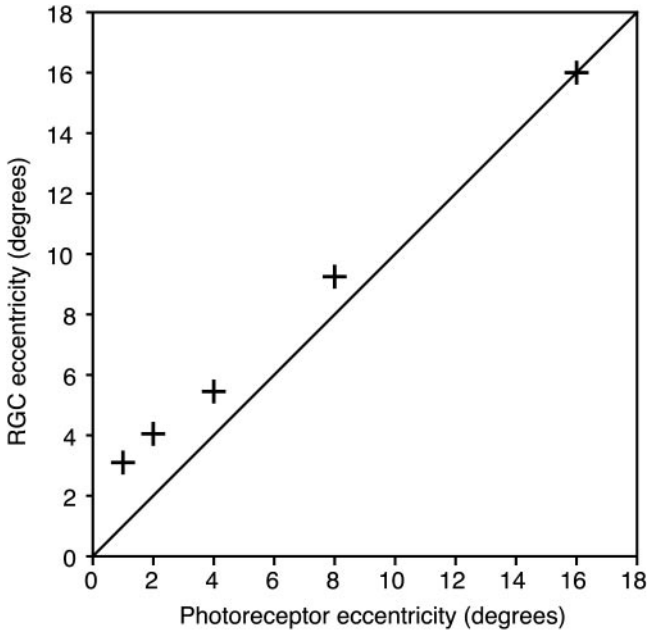

Figure 16. Eccentricity plot of photoreceptors versus corresponding ganglion cells. The solid line represents zero relative displacement. In the macula the ganglion cells are displaced centrifugally relative to their photoreceptors, accounting for the deviation of points from the solid line. By 16° the ganglion cells are centered over the photoreceptors that supply them.

situated in the macula as compared with ganglion cells located in the periphery.

Accuracy of the retinotopic map

The precision of our map was obtained by matching a large number (ranging between 55 and 89) of corresponding retinal and cortical points in each hemisphere. The alignment was strengthened further by matching the curved line segments (usually blood vessels) connecting retinal points to their cortical representation. The mean map (Fig. 3) was based on a total retinal/cortical match of 295 points and 310 line segments. Because the map was essentially a metabolic imprint of the retina, there was no relative error in location between points. In contrast, maps derived from microelectrode sampling have the problems of residual eye movements, receptive field scatter, inaccuracy in plotting receptive field centers, and difficulty in reconstructing electrode tracks. These factors combine to create error in the location of each retinotopic point, and this error varies unpredictably from point to point.

Our retinotopic map contained several potential sources of error peculiar to our approach. The process of rendering the folded occipital lobe into a flat-mount creates distortion. This distortion is minimal, because the preparation of a flat-mount entails unfolding, with little stretching or compressing, but some local distortion must occur. We have no good way to measure this distortion. Ideally, one might place a flexible grid pattern over the cortical surface of the flat-mount, fold it back up to resemble its original shape, and see how the grid pattern is distorted. Short of performing such an experiment, we can say only that too much distortion simply causes the tissue to tear, creating a natural relieving cut. With practice, one can flatten V1 with no tears, indicating that the tissue is not being deformed excessively.

The calibration of each retina was achieved by projecting the location of ~15 separate retinal landmarks onto a tangent screen, each with an error of ± 0.1°. This accuracy was achieved by using a fundus camera, a method that is more precise than a reversing ophthalmoscope. A correction could be made to convert linear measurements on the tangent screen to eccentricity in degrees. Unfortunately, the squirrel monkey eye is small and could not be photographed readily beyond 24°. For placement of the 32 and 50° isoeccentricity rings, we were forced to rely on Drasdo's schematic eye, scaled from the human to the squirrel monkey. Because this schematic eye may not be perfectly accurate and the optics of the squirrel monkey and human eye likely differ, this extrapolation probably introduced a small error. However, the peripheral retina is compressed into a small region of cortex, so a minor error in the location of these isoeccentricity rings could not have resulted in a displacement of more than a few hundred micrometers in the cortical map. Another potential error stemmed from our reliance on optical measurements to conclude that the monocular crescent begins at 72°. A behavioral measurement in an alert, trained monkey might have been more accurate.

The biggest source of error in our map resulted from the fact that blood vessels in the central 4° of the retina could not be discerned in the cortex. To fill this area, we inserted Cowey's map (1964) of the exposed cortical surface in the squirrel monkey. Fortuitously, this region corresponds to the central 4° of the visual hemifield, so it enabled us to localize the 1, 2, and 4° rings. Cowey's map was based on dozens of points sampled in a total of 47 monkeys. It is much easier to map accurately exposed cortex than buried cortex. For these reasons we believe his map is highly reliable. It was drawn, however, on a rear surface view of the intact occipital lobe. The shape of our flat-mount was slightly different, requiring a judgment about the best fit in transferring the map. This introduced uncertainty, especially in the location of the horizontal meridian. In our map it was placed in a position that did not divide the central 4° into equal upper and lower quadrants. Instead, the upper field representation occupied 122 mm^2 (58%), and the lower field representation occupied 89 mm^2 (42%). This discrepancy was caused by difficulty amalgamating our map with Cowey's and accounts for the higher anisotropy index of the lower field representation within the central 4° in Figure 6 as well as the higher density of patches shown within this sector in Figure 10.

Previous investigations have concluded that the lower field representation occupies more cortex than the upper field representation (Van Essen et al., 1984; Tootell et al., 1988). In humans the visual acuity, contrast sensitivity, temporal resolution, and reaction time are slightly better in the lower visual field (Low, 1943; Payne, 1965; Millodot and Lamont, 1974; Skrandies, 1985a,b). It is tempting to infer that these differences are attributable to greater cortical representation of the lower visual field. However, beyond 8° we found no difference in the areas occupied by the upper and lower visual fields. We found no evidence, either, for an enlarged representation of the lower visual field in the central 4°. Admittedly, our data could be biased because we may have mislocated the horizontal meridian in the central field slightly, as stipulated in the preceding paragraph. On the other hand, Van Essen and colleagues sampled large regions quite sparsely in their electrophysiological map [see Van Essen et al. (1984), their Fig. 5], and the deoxyglucose images of Tootell and colleagues lack a wedge of lower operculum containing upper field representation [see Tootell et al. (1988), their Fig. 3]. Given these uncertainties, we believe that it is premature to conclude that any asymmetry exists in upper versus lower field representations.

Table 1. Comparison of RGC and V1 parameters as a function of eccentricity

Eccentricity belt	Retinal ganglion cell density after displacement (cells/mm^2)	Number of retinal ganglion cells	Total retinal ganglion cells (%)	Striate cortex area (mm^2)	Total striate cortex area (%)
0–1°	301,235	25,605	2.5	49.3	6.3
1–2°	137,727	35,258	3.4	64.9	8.3
2–4°	64,917	66,280	6.4	97.3	12.5
4–8°	46,548	190,240	18.2	164.5	21.1
8–16°	7934	122,958	11.8	168.2	21.6
16–24°	5082	169,777	16.3	85.3	11.0
24–32°	3347	134,757	12.9	43.7	5.6
32–50°	1942	182,859	17.5	63.9	8.2
50–72°	1282	114,966	11.0	41.4	5.3
Total		1,057,184	100	778.3	100

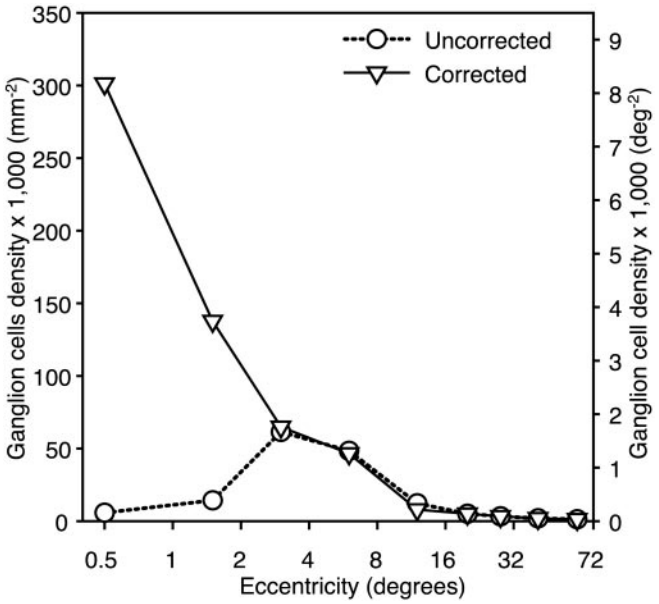

Figure 17. Plot of effective ganglion cell density after correction for eccentric displacement in the retina, showing a huge peak at the fovea. The dashed line shows the unshifted ganglion cell density, replotted from Figure 14.

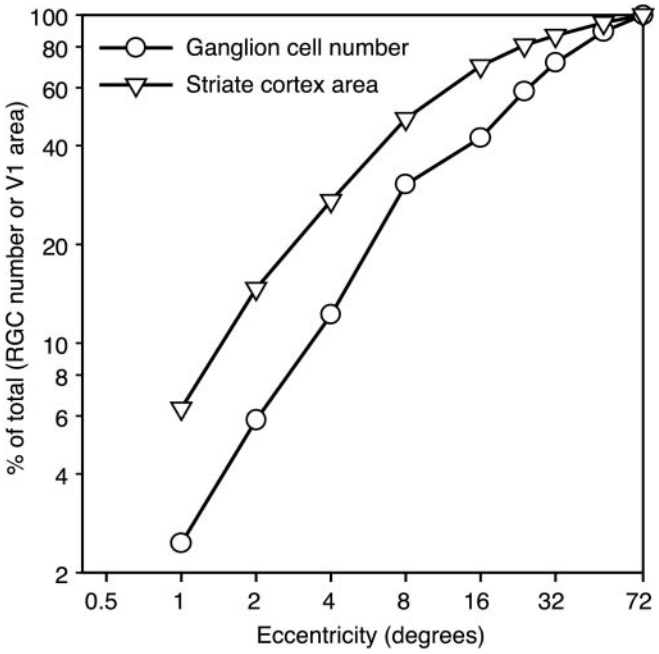

Figure 18. Log–log plot showing the cumulative percentage of ganglion cells and cortical surface area from the fovea to each eccentricity. Note that at central eccentricities the percentage of cortical surface area exceeds by twofold the percentage of retinal ganglion cells. Therefore, relative to its number of ganglion cells, the central visual field is "over-represented" in striate cortex.

Magnification factor

Calculation of cortical magnification across the visual field revealed how M_a, M_e, and M_p vary with eccentricity. We compared their functions with those predicted from the "complex log" map (for review, see Schwartz, 1984). The latter was found to fit well the average isopolar magnification factor (Fig. 4*B*). However, the cortex differed from the shape predicted by the complex log model (Fig. 5), because the upper and lower vertical meridia converged peripherally. As a result, the complex log model overestimated M_a and M_e peripherally (Fig. 4*A*, *C*).

Cortical anisotropy occurs when M_p and M_e are unequal locally. A perfectly conformal map has no local anisotropy. The anisotropy map (Fig. 6) showed that M_p tends to be greater than M_e along the vertical meridian and in the far periphery, owing to the shape of the cortex. Interestingly, the local variations of M_p and M_e combine so that M_a remains approximately constant as a function of polar angle at each eccentricity (Fig. 7*B*).

Retinal ganglion cells

The central visual field occupies a huge portion of striate cortex. This phenomenon arises, to some extent, from the high density of ganglion cells in the macula. Our data show, however, that even more cortex is allocated to the macula than one would expect from its concentration of ganglion cells (Fig. 18). Thus there is not a constant relationship between ganglion cell density and M_a from fovea to periphery. Instead, relatively more cortex is available for analysis of signals originating from central ganglion cells. This explains, in part, why macular cortex is labeled more faintly after intraocular [^{3}H]proline injection than peripheral cortex [see Adams and Horton (2002), their Fig. 3].

Previous investigators (Malpeli and Baker, 1975; Myerson et al., 1977; Perry and Cowey, 1985; Silveira et al., 1989, 1993; Azzopardi and Cowey, 1993, 1996; Popovic and Sjöstrand, 2001) have arrived at this conclusion. It has been questioned by others (Albus, 1975; Schein and de Monasterio, 1987; Wässle et al., 1989, 1990), who have argued for the principle that ganglion cells supply the same cortical territory at all eccentricities. If our cortical map is accurate, the only important source of potential error lies in our measurement of ganglion cell density. An underestimate centrally, or an overestimate peripherally, might have led us astray. As mentioned in Materials and Methods, maintaining our retinal whole mount in a hydrated state made it possible to count accurately the small, densely packed ganglion cells in the macula. Thus we do not believe that we undercounted ganglion cells centrally. To avoid overestimating their density peripherally, we used GABA immunohistochemistry to identify displaced amacrine cells. We found that 22–27% of neurons in the peripheral retina were GABA-positive, in agreement with a previous study that found 20% of cells GABA-positive at 50° (Koontz et al., 1993). In contrast, Wässle et al. (1990) found that displaced amacrine cells outnumbered ganglion cells by a factor of 5 in the peripheral temporal retina. This surprisingly high ratio resulted in a low

figure for peripheral ganglion cell density, leading the authors to conclude that there is no selective amplification of the macula in the cortex.

Correction for the centrifugal displacement of ganglion cells from photoreceptors introduces another potential source of error in calculating the allocation of cortical territory to ganglion cells. However, even a large error would not undermine our basic conclusion that central vision is over-represented. By 8° eccentricity the ganglion cells are nearly back in register with their photoreceptors. The central 8° contain 28% of the ganglion cells but correspond to 48% of the cortex (Table 1). Thus, ignoring the relative displacement of ganglion cells within the central 8°, one can see that this subpopulation of ganglion cells, taken as a whole, is over-represented in the cortex.

Approximately 10% of ganglion cells project to other targets than the lateral geniculate nucleus (Schiller and Malpeli, 1977; de Monasterio, 1978a,b; Perry and Cowey, 1984; Perry et al., 1984). If these nongeniculate targets place less emphasis on central vision, a greater percentage of peripheral ganglion cells may project to them. This source of potential error is small, however, because the overwhelming majority of ganglion cells projects to the lateral geniculate body. We recalculated our ganglion cells densities, assuming a "worst case scenario" (namely, that all nongeniculate projections come from peripheral retina), and found only a modest shift in the ratio between ganglion cell density and M_a, leaving our basic conclusion unchanged.

Strict scaling of cortical magnification factor to the density of RGCs is an appealing principle. However, like many principles of biology, it is true only to a first approximation. We conclude that the macula occupies a disproportionate amount of the surface area of V1. This phenomenon implies that the cortex handles processing of the macula in a special manner, by according it extra tissue for sensory analysis. This is another of the many specialized features of the macula that has evolved to optimize acuity.

References

Abercrombie M (1946) Estimation of nuclear population from microtome sections. Anat Rec 94:239–247.

Adams DL, Horton JC (2002) Shadows cast by retinal blood vessels mapped in primary visual cortex. Science 298:572–576.

Albus K (1975) A quantitative study of the projection area of the central and the paracentral visual field in area 17 of the cat. I. The precision of the topography. Exp Brain Res 24:159–179.

Allman JM, Kaas JH (1971) Representation of the visual field in striate and adjoining cortex of the owl monkey (*Aotus trivirgatus*). Brain Res 35:89–106.

Azzopardi P, Cowey A (1993) Preferential representation of the fovea in the primary visual cortex. Nature 361:719–721.

Azzopardi P, Cowey A (1996) The over-representation of the fovea and adjacent retina in the striate cortex and dorsal lateral geniculate nucleus of the macaque monkey. Neuroscience 72:627–639.

Bennett AG, Rudnicka AR, Edgar DF (1994) Improvements on Littmann's method of determining the size of retinal features by fundus photography. Graefes Arch Clin Exp Ophthalmol 232:361–367.

Blasdel G, Campbell D (2001) Functional retinotopy of monkey visual cortex. J Neurosci 21:8286–8301.

Boycott BB, Hopkins JM, Sperling HG (1987) Cone connections of the horizontal cells of the rhesus monkey's retina. Proc R Soc Lond [Biol] 229:345–379.

Brecha N (1983) Retinal neurotransmitters: histochemical and biochemical studies. In: Chemical neuroanatomy (Emson PC, ed), pp 85–129. New York: Raven.

Carroll EW, Wong-Riley MT (1984) Quantitative light and electron microscopic analysis of cytochrome oxidase-rich zones in the striate cortex of the squirrel monkey. J Comp Neurol 222:1–17.

Cowey A (1964) Projection of the retina on to striate and prestriate cortex in the squirrel monkey, *Saimiri sciureus*. J Neurophysiol 27:366–393.

Crooks J, Kolb H (1992) Localization of GABA, glycine, glutamate, and tyrosine hydroxylase in the human retina. J Comp Neurol 315:287–302.

Curcio CA, Allen KA (1990) Topography of ganglion cells in human retina. J Comp Neurol 300:5–25.

Curcio CA, Packer O, Kalina RE (1987) A whole-mount method for sequential analysis of photoreceptor and ganglion cell topography in a single retina. Vision Res 27:9–15.

Daniel PM, Whitteridge D (1961) The representation of the visual field on the cerebral cortex in monkeys. J Physiol (Lond) 159:203–221.

DeBruyn EJ, Wise VL, Casagrande VA (1980) The size and topographic arrangement of retinal ganglion cells in the galago. Vision Res 20:315–327.

de Monasterio FM (1978a) Properties of concentrically organized X and Y ganglion cells of macaque retina. J Neurophysiol 41:1394–1417.

de Monasterio FM (1978b) Properties of ganglion cells with atypical receptive-field organization in retina of macaques. J Neurophysiol 41:1435–1449.

DeYoe EA, Carman GJ, Bandettini P, Glickman S, Wieser J, Cox R, Miller D, Neitz J (1996) Mapping striate and extrastriate visual areas in human cerebral cortex. Proc Natl Acad Sci USA 93:2382–2386.

Dow BM, Snyder AZ, Vautin RG, Bauer R (1981) Magnification factor and receptive field size in foveal striate cortex of the monkey. Exp Brain Res 44:213–228.

Drasdo N, Fowler CW (1974) Non-linear projection of the retinal image in a wide-angle schematic eye. Br J Ophthalmol 58:709–714.

Engel SA, Glover GH, Wandell BA (1997) Retinotopic organization in human visual cortex and the spatial precision of functional MRI. Cereb Cortex 7:181–192.

Farias MF, Gattass R, Piñón MC, Ungerleider LG (1997) Tangential distribution of cytochrome oxidase-rich blobs in the primary visual cortex of macaque monkeys. J Comp Neurol 386:217–228.

Fischer B (1973) Overlap of receptive field centers and representation of the visual field in the cat's optic tract. Vision Res 13:2113–2120.

Fox PT, Miezin FM, Allman JM, Van Essen DC, Raichle ME (1987) Retinotopic organization of human visual cortex mapped with positron emission tomography. J Neurosci 7:913–922.

Frisén L, Schöldström G (1977) Relationship between perimetric eccentricity and retinal locus in a human eye. Comparison with theoretical calculations. Acta Ophthalmol (Copenh) 55:63–68.

Glickstein M, Fahle M (2000) Visual disturbances following gunshot wounds of the cortical visual area: based on observations of the wounded in the recent Japanese wars: 1900, 1904–05. Brain 123:1–101.

Grünert U, Wässle H (1990) GABA-like immunoreactivity in the macaque monkey retina: a light and electron microscopic study. J Comp Neurol 297:509–524.

Hendrickson A, Ryan M, Noble B, Wu JY (1985) Colocalization of [^{3}H]muscimol and antisera to GABA and glutamic acid decarboxylase within the same neurons in monkey retina. Brain Res 348:391–396.

Hendry SH, Schwark HD, Jones EG, Yan J (1987) Numbers and proportions of GABA-immunoreactive neurons in different areas of monkey cerebral cortex. J Neurosci 7:1503–1519.

Holden AL, Fitzke FW (1988) Image size in the fundus: structural evidence for wide-field retinal magnification factor. Br J Ophthalmol 72:228–230.

Holmes G, Lister WT (1916) Disturbances of vision from cerebral lesions, with special reference to the cortical representation of the macula. Brain 39:34.

Horton JC (1984) Cytochrome oxidase patches: a new cytoarchitectonic feature of monkey visual cortex. Philos Trans R Soc Lond [Biol] 304:199–253.

Horton JC, Hocking DR (1996a) Anatomical demonstration of ocular dominance columns in striate cortex of the squirrel monkey. J Neurosci 16:5510–5522.

Horton JC, Hocking DR (1996b) Intrinsic variability of ocular dominance column periodicity in normal macaque monkeys. J Neurosci 16:7228–7239.

Horton JC, Hocking DR (1998) Experimental strabismus reduces metabolic activity in ocular dominance columns serving the deviated eye. Soc Neurosci Abstr 24:105.105.

Horton JC, Hoyt WF (1991) The representation of the visual field in human

striate cortex: a revision of the classic Holmes map. Arch Ophthalmol 109:816–824.
Horton JC, Hubel DH (1981) Regular patchy distribution of cytochrome oxidase staining in primary visual cortex of macaque monkey. Nature 292:762–764.
Hubel DH, Freeman DC (1977) Projection into the visual field of ocular dominance columns in macaque monkey. Brain Res 122:336–343.
Hughes A (1976) A supplement to the cat schematic eye. Vision Res 16:149–154.
Inouye T (1909) Die Sehstörungen bei Schussverletzungen der kortikalen Sehsphäre nach Beobachtungen an Verwundeten der letzten japanischen Kriege. Leipzig: Engelmann.
Johnston A (1989) The geometry of the topographic map in striate cortex. Vision Res 29:1493–1500.
Kattah JC, Dennis P, Kolsky MP, Schellinger D, Cohan SL (1981) Computed tomography in patients with homonymous visual field deficits—a clinico-radiologic correlation. Comput Tomogr 5:301–312.
Kiernan JA (1990) Histological and histochemical methods: theory and practice, 2nd Ed. Oxford, UK: Pergamon.
Koontz MA, Hendrickson AE (1990) Distribution of GABA-immunoreactive amacrine cell synapses in the inner plexiform layer of macaque monkey retina. Vis Neurosci 5:17–28.
Koontz MA, Hendrickson AE, Ryan MK (1989) GABA-immunoreactive synaptic plexus in the nerve fiber layer of primate retina. Vis Neurosci 2:19–25.
Koontz MA, Hendrickson LE, Brace ST, Hendrickson AE (1993) Immunocytochemical localization of GABA and glycine in amacrine and displaced amacrine cells of macaque monkey retina. Vision Res 33:2617–2628.
Lane BP, Europa DL (1965) Differential staining of ultrathin sections of Epon-embedded tissues for light microscopy. J Histochem Cytochem 13:579–582.
Lapuerta P, Schein SJ (1995) A four-surface schematic eye of macaque monkey obtained by an optical method. Vision Res 35:2245–2254.
LeVay S, Connolly M, Houde J, Van Essen DC (1985) The complete pattern of ocular dominance stripes in the striate cortex and visual field of the macaque monkey. J Neurosci 5:486–501.
Leventhal AG, Rodieck RW, Dreher B (1981) Retinal ganglion cell classes in the Old World monkey: morphology and central projections. Science 213:1139–1142.
Low FN (1943) The peripheral acuity of 100 subjects. Am J Physiol 140:83–88.
Malpeli JG, Baker FH (1975) The representation of the visual field in the lateral geniculate nucleus of *Macaca mulatta*. J Comp Neurol 161:569–594.
McAuley DL, Russell RW (1979) Correlation of CAT scan and visual field defects in vascular lesions of the posterior visual pathways. J Neurol Neurosurg Psychiatry 42:298–311.
Millodot M, Lamont A (1974) Peripheral visual acuity in the vertical plane. Vision Res 14:1497–1498.
Myerson J, Manis PB, Miezin FM, Allman JM (1977) Magnification in striate cortex and retinal ganglion cell layer of owl monkey: a quantitative comparison. Science 198:855–857.
Nishimura Y, Schwartz ML, Rakic P (1985) Localization of γ-aminobutyric acid and glutamic acid decarboxylase in rhesus monkey retina. Brain Res 359:351–355.
Payne WH (1965) Visual reaction times on a circle about the fovea. Science 155:481–482.
Perry VH, Cowey A (1984) Retinal ganglion cells that project to the superior colliculus and pretectum in the macaque monkey. Neuroscience 12:1125–1137.
Perry VH, Cowey A (1985) The ganglion cell and cone distributions in the monkey's retina: implications for central magnification factors. Vision Res 25:1795–1810.
Perry VH, Cowey A (1988) The lengths of the fibres of Henle in the retina of macaque monkeys: implications for vision. Neuroscience 25:225–236.
Perry VH, Oehler R, Cowey A (1984) Retinal ganglion cells that project to the dorsal lateral geniculate nucleus in the macaque monkey. Neuroscience 12:1101–1123.
Pointer JS (1986) The cortical magnification factor and photopic vision. Biol Rev Camb Philos Soc 61:97–119.
Polyak SL (1941) The retina: the anatomy and the histology of the retina in man, ape, and monkey, including the consideration of visual functions, the history of physiological optics, and the histological laboratory technique. Chicago: University of Chicago.
Popovic Z, Sjöstrand J (2001) Resolution, separation of retinal ganglion cells, and cortical magnification in humans. Vision Res 41:1313–1319.
Rosa MG, Casagrande VA, Preuss T, Kaas JH (1997) Visual field representation in striate and prestriate cortices of a prosimian primate (*Galago garnetti*). J Neurophysiol 77:3193–3217.
Schein SJ (1988) Anatomy of macaque fovea and spatial densities of neurons in foveal representation. J Comp Neurol 269:479–505.
Schein SJ, de Monasterio FM (1987) Mapping of retinal and geniculate neurons onto striate cortex of macaque. J Neurosci 7:996–1009.
Schiller PH, Malpeli JG (1977) Properties and tectal projections of monkey retinal ganglion cells. J Neurophysiol 40:428–445.
Schwartz EL (1977) Spatial mapping in the primate sensory projection: analytic structure and relevance to perception. Biol Cybern 25:181–194.
Schwartz EL (1980) Computational anatomy and functional architecture of striate cortex: a spatial mapping approach to perceptual coding. Vision Res 20:645–669.
Schwartz EL (1983) Cortical mapping and perceptual invariance: a reply to Cavanagh. Vision Res 23:831–835.
Schwartz EL (1984) Computational studies of the spatial architecture of primate visual cortex. In: Primary visual cortex in primates (Peters A, Rockland KS, eds), pp 359–411. New York: Plenum.
Sereno MI, Dale AM, Reppas JB, Kwong KK, Belliveau JW, Brady TJ, Rosen BR, Tootell RB (1995) Borders of multiple visual areas in humans revealed by functional magnetic resonance imaging. Science 268:889–893.
Silveira LC, Picanco-Diniz C, Sampaio LF, Oswaldo-Cruz E (1989) Retinal ganglion cell distribution in the cebus monkey: a comparison with the cortical magnification factors. Vision Res 29:1471–1483.
Silveira LC, Perry VH, Yamada ES (1993) The retinal ganglion cell distribution and the representation of the visual field in area 17 of the owl monkey, *Aotus trivirgatus*. Vis Neurosci 10:887–897.
Skrandies W (1985a) Human contrast sensitivity: regional retinal differences. Hum Neurobiol 4:97–99.
Skrandies W (1985b) Critical flicker fusion and double flash discrimination in different parts of the visual field. Int J Neurosci 25:225–231.
Spalding JMK (1952) Wounds of the visual pathway. II. The striate cortex. J Neurol Neurosurg Psychiatry 15:169–183.
Spector RH, Glaser JS, David NJ, Vining DQ (1981) Occipital lobe infarctions: perimetry and computed tomography. Neurology 31:1098–1106.
Stone J (1981) The whole-mount handbook: a guide to the preparation and analysis of retinal whole mounts. Sydney: Maitland.
Stone J, Johnston E (1981) The topography of primate retina: a study of the human, bushbaby, and New and Old World monkeys. J Comp Neurol 196:205–223.
Talbot SA, Marshall WH (1941) Physiological studies on neural mechanisms of visual localization and discrimination. Am J Ophthalmol 24:1255–1264.
Teuber HL, Battersby NS, Bender MF (1960) Visual field defects after penetrating missile wounds of the brain. Cambridge, MA: Harvard UP.
Tolhurst DJ, Ling L (1988) Magnification factors and the organization of the human striate cortex. Hum Neurobiol 6:247–254.
Tootell RB, Switkes E, Silverman MS, Hamilton SL (1988) Functional anatomy of macaque striate cortex. II. Retinotopic organization. J Neurosci 8:1531–1568.
Van Essen DC, Newsome WT, Maunsell JH (1984) The visual field representation in striate cortex of the macaque monkey: asymmetries, anisotropies, and individual variability. Vision Res 24:429–448.
Wässle H, Chun MH, Müller F (1987) Amacrine cells in the ganglion cell layer of the cat retina. J Comp Neurol 265:391–408.
Wässle H, Grünert U, Röhrenbeck J, Boycott BB (1989) Cortical magnification factor and the ganglion cell density of the primate retina. Nature 341:643–646.
Wässle H, Grünert U, Röhrenbeck J, Boycott BB (1990) Retinal ganglion cell density and cortical magnification factor in the primate. Vision Res 30: 1897–1911.